

Active sensing ultrasonic guided wave-based damage diagnosis via stochastic stationary time-series models

Structural Health Monitoring
 2024, Vol. 23(4) 2559–2595
 © The Author(s) 2023
 Article reuse guidelines:
sagepub.com/journals-permissions
 DOI: 10.1177/14759217231201975
journals.sagepub.com/home/shm



Shabbir Ahmed and Fotis Kopsaftopoulos

Abstract

In the context of acousto-ultrasonic guided wave-based structural health monitoring, a statistical damage detection and identification (collectively referred to as damage diagnosis) framework for metallic and composite materials is proposed. Stochastic stationary time-series autoregressive (AR) models are used to model the ultrasonic wave propagation between piezoelectric actuator-sensor pairs on structural components and enable the damage diagnosis process via the use of the AR estimated parameters and corresponding covariance matrices. The proposed method exploits guided wave signals including the reflection parts, and thus the extraction of the S_0 and/or A_0 modes is not necessary, while the statistical properties and variation of estimated model parameters with respect to damage intersecting and non-intersecting wave propagation paths are presented and assessed. To investigate the method's performance and robustness, two variations are proposed based on the singular value decomposition and principal component analysis. The obtained modified AR parameter vectors are then used to estimate appropriate statistical characteristic quantities used to enable the damage detection and identification tasks. The diagnosis is based on properly defined statistical hypotheses decision-making schemes and predetermined type I error probabilities. The performance and applicability of the method are explored experimentally via a series of tests on aluminum and composite coupons under various damage scenarios for damage intersecting and non-intersecting paths. The results of the present study demonstrated the effectiveness and robustness of the proposed modeling and diagnostic framework for guided wave-based damage diagnosis that can be implemented in a potentially automated way.

Important conventions and symbols

Definition is indicated by $\hat{=}$. Matrix transposition is indicated by the superscript T .

Bold-face upper/lower case symbols designate matrix/column-vector quantities, respectively.

A functional argument in parentheses designates the function of a real variable; for instance $P(x)$ is a function of the real variable x .

A functional argument in brackets designates the function of an integer variable; for instance $x[t]$ is a function of normalized discrete time ($t = 1, 2, \dots$). The conversion from discrete normalized time to analog time is based on $(t - 1)T_s$, with T_s designating the sampling period.

A hat designates an estimator/estimate; for instance $\hat{\theta}$ is an estimator/estimate of θ .

Introduction

Structural health monitoring (SHM) has the potential to ensure enhanced safety and increased reliability of

aerospace, mechanical, and civil structures. An SHM method involves the automatic extraction of damage-sensitive features or quantities from a series of periodic measurements coming from an array of permanently installed sensors on a structure/system and performing statistical analysis of these quantities to establish the current structural state of the system. With the recent emphasis on the cyber-physical systems paradigm, incorporating SHM methods in structural systems has

Intelligent Structural Systems Laboratory (ISSL), Department of Mechanical, Aerospace and Nuclear Engineering, Rensselaer Polytechnic Institute, Troy, NY, USA

Corresponding author:

Fotis Kopsaftopoulos, Intelligent Structural Systems Laboratory (ISSL), Department of Mechanical, Aerospace and Nuclear Engineering, Rensselaer Polytechnic Institute, 110 8th Street, Troy, NY 12180-3522, USA.
 Email: kopsaf@rpi.edu

become essential to ensure safe operation and enable the automated inspection for damage/flaws/defects during in-service use, that is, to impart diagnostic and self-sensing capabilities.¹ This approach will obviate the need for periodic or routine maintenance and provide room for shifting toward the condition-based maintenance paradigm.

SHM methods may be broadly classified as local (or “hotspot”) or global.^{2,3} For the local monitoring of a structure, a wide variety of methods are available based on ultrasound,^{3–5} eddy currents,⁶ acoustic emissions,⁷ and thermal field principles.⁸ On the other hand, the vibration-based family of methods is classified within the global monitoring category and uses random excitation/response signals combined with statistical model building, and statistical decision-making to diagnose the current health state of the structure/system.^{9–11} The idea behind the vibration-based approach is that small changes (defects and/or damage) in a structure induce changes in the vibration response signal(s), and these changes may be detected and correlated with a specific cause (damage).^{2,12,13} Although vibration-based methods are more robust in the face of environmental and operational conditions, they may be less sensitive to incipient (small) damage/defects and corresponding local effects. On the contrary, some of the local active sensing SHM approaches, such as ultrasonic guided wave-based methods, are highly sensitive to local effects and can detect minor structural changes.^{3,5,14} Such waves can easily be generated/collected by piezoelectric transducers in the form of an applied strain/voltage.^{15,16} Damage/health indices/indicators (D/HI) are widely used metrics for performing damage detection. The idea is that the features of the signal from an unknown structural state are compared to those coming from a healthy structure.^{17–23} These features are usually based on specific mode wave packets, such as the S_0 (symmetric) and A_0 (antisymmetric) modes of wave propagation signals, the amplitude/magnitude, or the energy content of the signal. These conventional damage index (DI)-based approaches are used for their damage/no-damage binary detection paradigm and simplicity in decision-making that is oftentimes based on deterministic techniques and user-defined arbitrary thresholds. On the other hand, damage localization involves the identification of the geometric location of the damage within the structure.^{24,25}

The selection of an appropriate DI formulation may influence the diagnostic performance of an SHM system. The DI should be chosen in such a way that it is highly sensitive to the growth, size, and orientation of damage, and less sensitive to other external factors such as material property variations, the effect of adhesive, and lead zirconate titanate (PZT) placement.³ The majority of DI-based methods do not employ the

complete wave propagation signal but depend on the use of specific arrival wave packets, such as the ones corresponding to the S_0 and A_0 modes. However, the clear identification and separation of these waves is not always an easy task as the waves may overlap and cannot be clearly distinguished. To eliminate the limitations of conventional time-domain DIs, frequency-domain DIs^{26,27} or a combination of time-frequency (mixed-domain) DIs²⁸ have been proposed. By capitalizing on some nonlinear features of the guided wave signals and thus formulating nonlinear DIs, barely visible fatigue cracks can be detected.²⁹ It has also been reported that wavelet entropy-based detection and localization methods may offer improved performance compared to conventional time-of-arrival-based algorithms in the presence of damage.^{30,31} However, the majority of the DI formulations in the literature are deterministic in nature and require arbitrary, user-defined detection, and identification thresholds. Recently, steps have been taken toward formulating probabilistic DIs using Gaussian mixture models, Gaussian process regression, and other probabilistic or statistical tools.^{5,17,32,33} For the case of Gaussian mixture models, instead of comparing the individual healthy and damaged state DIs, their corresponding probability distributions are compared via the Kullback-Liebler divergence or appropriate modifications.³² However, such probabilistic DI-based formulations may show suboptimal performance if the reflections part of the guided wave signals is included in the analysis. In addition, these methods do not model the actual wave propagation patterns for different paths nor account for the underlying wave propagation dynamics. In this respect, the use of stochastic time-series models may be an appropriate alternative.^{17,34–37}

Stochastic time-series models have been widely used in the context of vibration-based damage diagnosis.^{2,13,38–43} Such models require data availability for their identification and parameter estimation and can enable statistical decision-making under uncertainty due to their stochastic nature and inherent modeling of noise and/or uncertainty. In addition, their identification is straightforward, they have compact representations, and the same models can be used for different structural components and host materials (both metallic and composites). When it comes to ultrasonic wave propagation, strictly speaking, guided waves can be considered nonstationary signals due to their dispersive nature and their variance evolving over time. Thus, to properly represent such waves, time-varying parametric time-series models seem a natural choice.^{34,44–46} However, due to the narrowband characteristics of such ultrasonic waves and their mild non-stationarity (the signal mean remains constant while the variance may evolve depending on the type and frequency of the

wave), and in the context of damage diagnosis, simpler stationary representations (time-invariant) can also be used without significant loss in modeling accuracy and robustness. Time-invariant statistical SHM parametric methods are based upon autoregressive moving average (ARMA) or related types and their extensions. These methods have attracted considerable attention and have been used extensively in analyzing low-frequency vibration responses excited by a random white noise actuation.^{2,11} However, these methods remain unexplored in the context of ultrasonic guided wave-based SHM, which traditionally exploits a narrowband high-frequency excitation for wave generation.

Recently, nonlinear autoregressive with exogenous excitation (NARX) models were introduced in the context of ultrasonic guided wave-based damage diagnosis.^{47,48} It was shown that instead of a single-step ahead prediction, a multi-step ahead prediction scheme with a suitable training procedure may improve the damage detection performance. Moreover, Da Silva et al.⁴⁹ have used a Gaussian process NARX model for performing damage detection in composite structures. However, unless there are evident nonlinearities in the wave propagation signals that need to be properly represented, NARX models require elaborate model structure selection techniques for properly capturing the nonlinear relationships between excitation and/or response waves, and representing the nonlinear dynamics; such elaborate approaches that pose additional modeling challenges may not be required to achieve effective damage diagnosis. In such cases, simpler linear time-invariant autoregressive (AR) counterparts may serve the purpose of damage diagnosis with high accuracy and robustness.

The main objective of this work is the postulation and performance assessment of a novel damage detection and identification (diagnosis) scheme using stationary stochastic time series, namely AR models in the context of the active sensing guided wave-based SHM. The key problems/challenges that the present study addresses and the advantages that the method offers are the following: (i) no need for the diagnostic process to rely on distinct wave packets, such as the S_0 and A_0 modes, and ignore reflections, which is the case for the vast majority of detection and localization methods. Having clearly distinguishable wave packets requires additional experiments to obtain the dispersion curves and decide on appropriate center frequencies for the wave's excitation. In addition, it is extremely challenging, if possible at all, to automate the process for the extraction of the S_0 and A_0 modes, especially in composite materials in which the direction of the wave propagation has a significant impact on the recorded signals. (ii) The proposed method is based on a statistical framework where the estimator asymptotic properties

are used to construct appropriate confidence intervals for the estimated model parameters. These intervals allow the construction of statistical thresholds for determining the existence and size of the damage. The majority of the literature on guided wave-based SHM employs user-defined, and thus arbitrary thresholds, for detecting, localizing, and quantifying damage. In addition, existing probabilistic methods are based on complex nonlinear model representations that exhibit unnecessary complexity,^{47,48} and Bayesian approaches that solve computationally costly inverse problems and/or require the use of multi-physics-based numerical models and various sampling approaches to determine the statistical distributions of the quantities of interest. (iii) The method currently postulated is relatively simple, computationally efficient, and can be easily automated without the need for user intervention. (iv) Various methods presented in the literature can be effective either on metallic or composite coupons, as they need to be tailored to the specific material properties and corresponding wave propagation patterns. (v) The proposed method is based on time-series models that offer insight into the wave propagation dynamics, underlying modal characteristics (natural frequencies, damping ratios), and uncertainty/noise levels, thus allowing for interpretable results. This is not the case when it comes to machine learning (ML) methods employing deep neural networks or other architectures (convolutional neural networks, recurrent neural networks (RNNs)). Such models and methods may provide accurate signal representation; however, there is no engineering/physical insight into the wave propagation patterns, and therefore they lack explainability. (vi) Finally, the identification and parameter estimation of AR models is simple as it is based on computationally efficient closed-form solutions realized by least squares estimators (that can be shown to be the best linear unbiased estimators coinciding with the maximum likelihood estimator). Moreover, the model structure selection and validation are based on established statistical criteria. This is not the case for ML-based methods, which may require extensive training and large data sets with no guarantees of optimal model architecture selection.

A preliminary study on this topic using AR models for isotropic materials was performed by Ahmed et al.³⁷ Early studies by the authors on damage detection and identification using stochastic time-varying models were also recently presented in a series of conference papers.^{36,50–52} In the present study, the complete formulation of the stochastic time-series model-based framework for active sensing SHM is presented along with two variations based on singular value decomposition (SVD) and principal component analysis (PCA) schemes. A comprehensive study is presented on the

method's characteristics and performance given the achieved damage detection accuracy and robustness. An experimental assessment is presented via two test cases on aluminum and composite coupons and results are presented and discussed with respect to damage intersecting and non-intersecting paths. A comparison with traditional deterministic tone-burst actuation and DI-based methods is also presented to demonstrate and evaluate the performance of the proposed methods. The main novel aspects of this study include:

- Introduction of stochastic time-series models for representing ultrasonic wave propagation and tackling damage detection and identification in active sensing guided wave-based SHM.
- Use of the complete signal in the modeling and diagnostic stages, including the reflections part, rather than specific S_0 and/or A_0 modes or the non-reflecting part of the signals.
- Use of SVD and PCA techniques on model parameters for reducing the dimensionality of the damage-sensitive parameters, improving the classification capability, and assessing the diagnostic performance.
- Extraction and use of both theoretical asymptotic and experimental parameter covariance matrices, confidence bounds of the model parameters, and formulation of a damage diagnosis scheme (damage detection and identification) based on statistical hypothesis testing for decision-making.
- Application of the proposed method in two different types of coupons: an aluminum plate and a composite plate. That is, the same method applies to both metals and composites alike.

The remainder of this article is organized as follows: the section “Stochastic time-series models for wave propagation” introduces the stochastic modeling of guided wave signals using AR models and the process of model identification. Section “Damage diagnosis via stochastic autoregressive models” presents the theory of three statistical damage diagnosis schemes based on estimated AR model parameters while section “The damage diagnosis framework” presents the damage diagnosis framework. Then, the experimental setup, path selection, results, and discussion are presented for aluminum and composite plate in sections “Test case I: aluminum plate with simulated damage” and “Test case II: CFRP plate with simulated damage”, respectively. Finally, the section “Discussion” summarizes the main conclusions and comments on future research directions.

Stochastic time-series models for wave propagation

Guided waves propagating on structural host materials can be considered nonstationary signals due to their dispersive nature. However, in cases with mild non-stationarity (the signal mean remains constant while the variance may exhibit time-dependent variations depending on the actuation characteristics and material properties), time-invariant AR models offer an effective modeling approach based on statistical estimation techniques and corresponding asymptotic properties that may enable accurate and robust damage diagnosis.² In this study, AR models are used to represent the guided wave propagation signals between piezoelectric actuator-sensor pairs and enable the damage detection and identification tasks.

An AR(na) model can be expressed in the following form^{2,53}:

$$y[t] + \sum_{i=1}^{na} a_i \cdot y[t-i] = e[t] \quad e[t] \sim \text{iid } \mathcal{N}(0, \sigma_e^2) \quad (1)$$

with t designating the normalized discrete time ($t = 1, 2, 3, \dots$ with absolute time being $(t-1)T_s$, where T_s stands for the sampling period), $y[t]$ the measured guided wave response signals as generated by the piezoelectric sensors on the structure, na the AR model order, and $e[t]$ the innovations (also referred to as residual or one-step-ahead prediction error) sequence. It is assumed that the residual sequence $e[t]$ is white (serially uncorrelated), Gaussian, with zero mean and variance σ_e^2 . The symbol $\mathcal{N}(\cdot, \cdot)$ designates Gaussian distribution with the indicated mean and variance, and iid stands for identically independently distributed.

The one-step-ahead prediction $\hat{y}[t/t-1]$ of the signal value $y[t]$ made at time $t-1$ (i.e., for given values of the signal up to time $t-1$) can be given as (a hat designates estimator/estimate; for instance, $\hat{\theta}$ is an estimator/estimate of θ):

$$\hat{y}[t/t-1] = - \sum_{i=1}^{na} a_i \cdot y[t-i] \quad (2)$$

Comparing Equation (2) with the AR model Equation (1), it is evident that the one-step-ahead prediction error is equal to $e[t]$, that is:

$$\hat{e}[t/t-1] \stackrel{\Delta}{=} y[t] - \hat{y}[t/t-1] = e[t]. \quad (3)$$

Using the backshift operator $\mathcal{B}(\mathcal{B}^i \cdot y[t] \stackrel{\Delta}{=} y[t-i])$, the AR representation of Equation (1) may be compactly re-written as:

$$y[t] + \sum_{i=1}^{na} a_i \cdot \mathcal{B}^i \cdot y[t] = e[t] \Leftrightarrow A[\mathcal{B}] \cdot y[t] = e[t], \quad e[t] \sim \text{iid } \mathcal{N}(0, \sigma_e^2) \quad (4)$$

with

$$A[\mathcal{B}] = 1 + \sum_{i=1}^{na} a_i \cdot \mathcal{B}^i. \quad (5)$$

The model identification problem is usually distinguished into two subproblems: (i) the *parameter estimation* and (ii) the *model structure selection*, presented in sections “Model parameter estimation” and “Model structure selection”, respectively.

Model parameter estimation

The AR model of Equation (1) can be parameterized in terms of the parameter vector $\boldsymbol{\theta} = [a_1 \dots a_{na}; \sigma_e^2]^T$ to be estimated from the measured signals and may be written in linear regression form as:

$$y[t] = \boldsymbol{\phi}^T[t] \cdot \boldsymbol{\theta} + e[t] \quad (6)$$

with

$$\boldsymbol{\phi}[t] = [-y[t-1] - y[t-2] \dots - y[t-na]]^T \text{ and } \boldsymbol{\theta} = [a_1 \dots a_{na}]^T_{[na \times 1]} \quad (7)$$

and T designating transposition. Then, following the substitution of the data for $t = 1, 2, \dots, N$, the following expression is obtained:

$$\mathbf{y} = \boldsymbol{\phi} \cdot \boldsymbol{\theta} + \mathbf{e} \quad (8)$$

where

$$\mathbf{y} := \begin{bmatrix} y[1] \\ \vdots \\ y[N] \end{bmatrix} \quad \boldsymbol{\phi} := \begin{bmatrix} \boldsymbol{\phi}[1] \\ \vdots \\ \boldsymbol{\phi}[N] \end{bmatrix} \quad \mathbf{e} := \begin{bmatrix} e[1] \\ \vdots \\ e[N] \end{bmatrix}. \quad (9)$$

Using the above linear regression framework, the estimation of the parameter vector $\boldsymbol{\theta}$ is based on the minimization of the weighted least squares (WLS) criterion (a more appropriate criterion compared to ordinary least squares in view of the Gauss–Markov theorem):

$$J^{\text{WLS}} = \frac{1}{N} \sum_{t=1}^N e^T[t] \boldsymbol{\Gamma}_{e[t]}^{-1} e[t] = \frac{1}{N} \mathbf{e}^T \boldsymbol{\Gamma}_e^{-1} \mathbf{e} \quad (10)$$

which leads to the WLS estimator:

$$\hat{\boldsymbol{\theta}}^{\text{WLS}} = [\boldsymbol{\phi}^T \boldsymbol{\Gamma}_e^{-1} \boldsymbol{\phi}]^{-1} [\boldsymbol{\phi}^T \boldsymbol{\Gamma}_e^{-1} \mathbf{y}]. \quad (11)$$

In these expressions, $\boldsymbol{\Gamma}_e = E\{\mathbf{e} \mathbf{e}^T\}$ is the residual covariance matrix, which is practically unavailable. Nevertheless, it may be consistently estimated by applying ordinary least squares in the first step. Once the $\hat{\boldsymbol{\theta}}^{\text{WLS}}$ has been obtained, the final residual and residual variance can be obtained by:

$$e[t] = y[t] - \boldsymbol{\phi}^T[t] \cdot \hat{\boldsymbol{\theta}}^{\text{WLS}} \text{ and } \hat{\sigma}_e^2(\hat{\boldsymbol{\theta}}^{\text{WLS}}) = \frac{1}{N} \sum_{t=1}^N e^2[t, \hat{\boldsymbol{\theta}}^{\text{WLS}}]. \quad (12)$$

The estimator $\hat{\boldsymbol{\theta}}^{\text{WLS}}$ may, under mild conditions, be shown to be asymptotically Gaussian distributed with mean coinciding with the true parameter vector $\boldsymbol{\theta}^o$ and covariance matrix $\mathbf{P}_{\boldsymbol{\theta}}$:

$$\sqrt{N}(\hat{\boldsymbol{\theta}}_N - \boldsymbol{\theta}^o) \sim \mathcal{N}(\boldsymbol{\theta}, \mathbf{P}_{\boldsymbol{\theta}}) \quad \text{as } N \rightarrow \infty. \quad (13)$$

This is an important property that will be used for the formulation of appropriate statistical hypothesis testing procedures for decision-making and damage diagnosis.

Model structure selection

Model structure selection entails the selection of the AR model order na . Trial-and-error or successive fitting schemes may be employed for this purpose,⁵⁴ where models corresponding to various candidate structures, that is, models with different na values are estimated, and the one providing the best fitness to the signal is selected. The choice of the fitness function may depend on the specific task at hand. A usual choice is the Gaussian log-likelihood function of each candidate model. The particular model structure that maximizes the log-likelihood is the most likely to be the actual underlying model responsible for the generation of the measured signal. However, a problem with this approach is that the log-likelihood may be monotonically increasing with increasing model orders, and as a result, the overfitting of the measured signal occurs. For this reason, criteria such as the AIC (Akaike information criterion⁵⁵) or the BIC (Bayesian information criterion⁵⁶) are generally used and can be represented as follows:

$$\text{AIC} = -2 \cdot \ln \mathcal{L}(\mathcal{M}(\boldsymbol{\theta}, \sigma_e^2) | \mathbf{y}^N) + 2 \cdot d \quad (14)$$

$$\text{BIC} = -\ln \mathcal{L}(\mathcal{M}(\boldsymbol{\theta}, \sigma_e^2) | \mathbf{y}^N) + \frac{\ln N}{2} \cdot d \quad (15)$$

with \mathcal{L} designating the model likelihood, N the number of signal samples, and d the number of independently estimated model parameters. As it may be observed, both criteria consist of a superposition of the negative log-likelihood function and a term that penalizes the

model order, or structural complexity, and thus discourages the model overfitting. Accordingly, the model that minimizes the AIC or the BIC is selected. The ratio of the residual sum of squares versus the signal sum of squares (RSS/SSS) may also be used as another fitness criterion for selecting the best model.

Damage diagnosis via stochastic autoregressive models

The damage detection and identification of a structure can be based on a characteristic quantity $Q = f(\boldsymbol{\theta})$, which is a function of the parameter vector $\boldsymbol{\theta}$ of an AR model. Three approaches that were investigated in this work are described next.

Standard model parameter approach

The parameter vector $\boldsymbol{\theta}$ can be estimated by the asymptotically efficient WLS estimator and is designated as $\hat{\boldsymbol{\theta}}$. The estimated parameter vector $\hat{\boldsymbol{\theta}}$ is Gaussian distributed with a mean equal to its true value $\boldsymbol{\theta}$ and a certain covariance $\mathbf{P}_{\boldsymbol{\theta}}$ ($\hat{\boldsymbol{\theta}} \sim \mathcal{N}(\boldsymbol{\theta}, \mathbf{P}_{\boldsymbol{\theta}})$).

Damage detection is based on testing for statistically significant changes in the parameter vector $\boldsymbol{\theta}$ between the nominal and current state of the structure through the hypothesis testing problem.

$$H_0 : \delta\boldsymbol{\theta} = \boldsymbol{\theta}_o - \boldsymbol{\theta}_u = 0 \quad \text{null hypothesis - healthy structure} \quad (16)$$

$$H_1 : \delta\boldsymbol{\theta} = \boldsymbol{\theta}_o - \boldsymbol{\theta}_u \neq 0 \quad \text{alternative hypothesis} \quad (17) \\ \quad \text{-- damaged structure}$$

It is to be mentioned here that $\boldsymbol{\theta}_o$ designates the parameter vector from the healthy structural state and $\boldsymbol{\theta}_u$ designates the parameter vector from the unknown structural state. The difference between the two parameter vector estimators also follows Gaussian distribution, that is, $\delta\hat{\boldsymbol{\theta}} = \hat{\boldsymbol{\theta}}_o - \hat{\boldsymbol{\theta}}_u \sim \mathcal{N}(\delta\boldsymbol{\theta}, \delta\mathbf{P})$, with $\delta\boldsymbol{\theta} = \boldsymbol{\theta}_o - \boldsymbol{\theta}_u$ and $\delta\mathbf{P} = \mathbf{P}_o + \mathbf{P}_u$, where \mathbf{P}_o , \mathbf{P}_u designate the corresponding covariance matrices. Under the null (H_0) hypothesis $\delta\hat{\boldsymbol{\theta}} = \hat{\boldsymbol{\theta}}_o - \hat{\boldsymbol{\theta}}_u \sim \mathcal{N}(0, 2\mathbf{P}_o)$ and the quantity

$$Q = (\delta\hat{\boldsymbol{\theta}})^T \cdot \delta\mathbf{P}^{-1} \cdot (\delta\hat{\boldsymbol{\theta}}) \quad \text{with } \delta\mathbf{P} = 2\mathbf{P}_o \quad (18)$$

follows a χ^2 distribution with $d = \dim(\boldsymbol{\theta})$ (parameter vector dimensionality) degrees of freedom. As the covariance matrix \mathbf{P}_o corresponding to the healthy structure is unavailable, its estimated version $\hat{\mathbf{P}}_o$ is used. The following equation is used for estimating the covariance matrix:

$$\hat{\mathbf{P}}_o = \frac{1}{N} \left\{ \frac{1}{N} \sum_{t=1}^N \frac{\boldsymbol{\phi}[t] \cdot \boldsymbol{\phi}^T[t]}{\hat{\sigma}_e^2} \right\}^{-1} \cdot \left\{ \frac{1}{N} \sum_{t=1}^N \frac{\sigma_e^2 \cdot \boldsymbol{\phi}[t] \cdot \boldsymbol{\phi}^T[t]}{\hat{\sigma}_e^4} \right\} \cdot \left\{ \frac{1}{N} \sum_{t=1}^N \frac{\boldsymbol{\phi}[t] \cdot \boldsymbol{\phi}^T[t]}{\hat{\sigma}_e^2} \right\}^{-1} \quad (19)$$

It is to be mentioned here that the estimated covariance matrix follows a d -variate Wishart distribution with $N - 1$ degrees of freedom. As a result, when the distribution of the estimated covariance is taken into account, the probability distribution of the characteristic quantity Q becomes Hotelling's T^2 distribution⁵⁷ [Chapter 3, pp. 85]:

$$Q = (\delta\hat{\boldsymbol{\theta}})^T \cdot (2\hat{\mathbf{P}}_o)^{-1} \cdot (\delta\hat{\boldsymbol{\theta}}) \in T_{d, N-1}^2 \quad (20) \\ \text{with } T_{d, N-1}^2 = \frac{d(N^2 - 1)}{N(N - d)} \sim \mathcal{F}(d, N - d)$$

where \mathcal{F} is Fisher's \mathcal{F} distribution with d and $N - d$ degrees of freedom in the section "Fisher's \mathcal{F} distribution". Note that, as $N \rightarrow \infty$, $\mathcal{F}(d, N - d)$ approaches $\chi^2(d)$ distribution. As a result, when the number of data points N is large, the use of χ^2 distribution for determining the critical limit is a good and valid approximation⁵³ [Appendix II, pp. 558].

Then the following test is constructed at the α (type I) risk level:

$$Q \leq \chi_{1-\alpha}^2(d) \Rightarrow H_0 \quad \text{is accepted (healthy structure)} \quad (21)$$

$$\text{Else} \Rightarrow H_1 \quad \text{is accepted (damaged structure)} \quad (22)$$

where $\chi_{1-\alpha}^2(d)$ designates the χ^2 distribution's $(1 - \alpha)$ critical points. Damage identification may be based on a multiple hypothesis testing problem comparing the parameter vector $\hat{\boldsymbol{\theta}}_u$ belonging to the current state of the structure to those corresponding to different damage types $\hat{\boldsymbol{\theta}}_A, \hat{\boldsymbol{\theta}}_B, \dots$

SVD-based approach

A simplified SVD-based method can also be used where eigen decomposition is performed on the diagonal matrix formed by the parameter vector. In this case, instead of projecting the parameter vector onto some lower-dimensional space, the relative importance of the parameters is determined and the important m parameters are kept while the rest are discarded.

The diagonal matrix formed by the parameter vector is decomposed in the following way:

$$\mathbf{D}(\hat{\boldsymbol{\theta}}_o) = \mathbf{C}\Lambda\mathbf{C}^{-1} \quad (23)$$

where

$$\Lambda = \begin{bmatrix} \lambda_1 & 0 & \cdots & 0 \\ 0 & \lambda_2 & \cdots & 0 \\ \vdots & \vdots & \ddots & \vdots \\ 0 & 0 & \cdots & \lambda_n \end{bmatrix} \quad (24)$$

$$C = [c_1 \ c_2 \ c_3 \ \cdots \ c_n] \quad (25)$$

The vectors c_1, c_2, \dots, c_n are the eigenvectors of the positive definite parameter matrix $D(\hat{\theta}_o)$ and the diagonal elements of Λ are the corresponding eigenvalues $\Lambda_{ii}=\lambda_i$. The diagonal elements can be extracted into a vector $e = \text{diag}(\Lambda)$, where

$$e = [\lambda_1, \lambda_2, \lambda_3, \dots, \lambda_n]. \quad (26)$$

In this case, the diagonal elements are not necessarily arranged in descending order. Moreover, each eigenvalue corresponds to a particular value of the parameter vector. Knowing this, the magnitude of the eigenvalues is arranged in descending order in the vector \hat{e} , with

$$\hat{e} = [\hat{\lambda}_1, \hat{\lambda}_2, \hat{\lambda}_3, \dots, \hat{\lambda}_n] \text{ with } \hat{\lambda}_1 \geq \hat{\lambda}_2 \geq \dots \geq \hat{\lambda}_n \quad (27)$$

and the corresponding model parameters become:

$$\theta_o^{\text{eig}} = [\hat{a}_1^{\hat{\lambda}_1}, \hat{a}_2^{\hat{\lambda}_2}, \hat{a}_3^{\hat{\lambda}_3}, \dots, \hat{a}_n^{\hat{\lambda}_n}]. \quad (28)$$

Now from this parameter vector, the first m parameters are chosen where $m < n$. As a result, the parameter vector and the associated covariance matrix for damage detection become:

$$\theta_o^{\text{eig}} = [\hat{a}_1^{\hat{\lambda}_1}, \hat{a}_2^{\hat{\lambda}_2}, \hat{a}_3^{\hat{\lambda}_3}, \dots, \hat{a}_m^{\hat{\lambda}_m}] \quad (29)$$

$$D(\hat{\theta}_o^{\text{eig}}) = \hat{C} \hat{\Lambda} \hat{C}^{-1} \quad (30)$$

with

$$\hat{\Lambda} = \begin{bmatrix} \hat{\lambda}_1 & 0 & \cdots & 0 \\ 0 & \hat{\lambda}_2 & \cdots & 0 \\ \vdots & \vdots & \ddots & \vdots \\ 0 & 0 & \cdots & \hat{\lambda}_m \end{bmatrix}. \quad (31)$$

PCA-based approach

In addition to using $d = \dim(\theta) = na$, a truncated version of the parameter vector θ may also be used to simplify the damage detection procedure. Because all of the parameters may not be equally sensitive to the damage and may introduce artifacts in the damage detection. To avoid that situation, a truncation approach based on PCA may be used. The idea is to project the baseline (healthy) parameter vector θ_o onto a

coordinate system where information compression is possible. A subspace of lower dimensionality, without sacrificing significant information, is subsequently selected, and the discrepancy between the baseline (healthy) and the current vector is projected onto the same subspace.

In the beginning, the covariance matrix is diagonalized via SVD as follows:

$$P(\hat{\theta}_o) = U \cdot S \cdot U^T \quad (32)$$

with

$$S = \begin{bmatrix} s_1 & 0 & \cdots & 0 \\ 0 & s_2 & \cdots & 0 \\ \vdots & \vdots & \ddots & \vdots \\ 0 & 0 & \cdots & s_n \end{bmatrix} \quad (33)$$

$$U = [u_1 \ u_2 \ u_3 \ \cdots \ u_n] \quad (34)$$

where U is an orthonormal matrix ($UU^T=I$), and the columns of which define the principal components and form a subspace spanning the vector θ_o . The singular values $s_j(j=1, 2, \dots, n)$ are ranked in decreasing order and represent the active energy of the associated principal components. The subspace dimensionality selection is then based on bounding the information loss, expressed in terms of active energy contribution, below a certain threshold. A measure of how well the first m principal components explain the variance of $\hat{\theta}_o$ is given by the relative proportion

$$\Psi_m = \frac{\sum_{j=1}^m s_j}{\sum_{j=1}^n s_j} 100(\%). \quad (35)$$

Selecting only the first m coordinates $\{u_1, u_2, \dots, u_m\}$ in Equation (35), an m -dimensional subspace is determined, and the projection of $\hat{\theta}_o$ on this subspace is given by:

$$\hat{\theta}_o^{\text{PCA}} = U_m^T \hat{\theta}_o \quad (36)$$

with

$$U_m = [u_1 \ u_2 \ u_3 \ \cdots \ u_m] \quad (37)$$

$$P(\hat{\theta}_o^{\text{PCA}}) = U_m^T P(\hat{\theta}_o) U_m = \begin{bmatrix} s_1 & 0 & \cdots & 0 \\ 0 & s_2 & \cdots & 0 \\ \vdots & \vdots & \ddots & \vdots \\ 0 & 0 & \cdots & s_m \end{bmatrix}. \quad (38)$$

The damage diagnosis framework

In this work, ultrasonic guided wave signals are collected from the structure in its healthy and damaged states. Then damage detection and identification are

performed by modeling the wave propagation signals through the AR models. Although guided wave signals are nonstationary in nature, however, in the case of weak non-stationarity, an AR model can be used for damage detection and identification.

To formulate the problem statement in a structured way, let S_v represent the structure under consideration. $v=o$ indicates a healthy state and any other v from the set $v=\{a, b, \dots\}$ indicates the damaged state of the structure. S_a, S_b, \dots , etc. represent a distinct type of damage with different magnitudes and characteristics.

Now the problem can be defined as: given the structure in its currently unknown state u , determine whether the structure is damaged or not ($u=o$ or $u \neq o$) from the available ultrasonic signals. This is known as the damage detection problem. In case, the structure is found to be damaged, determine the current damage type from the possible damage scenarios $\{a, b, \dots\}$. This is known as the damage identification problem.

Stochastic time-series models commonly use discretized excitation $x[t]$ and/or response $y[t]$ (for $t=1, 2, \dots, N$) signals. The complete excitation and response signals are represented as \mathbf{x} and \mathbf{y} , respectively, that is, $\mathbf{z}=[\mathbf{x}, \mathbf{y}]$. In the absence of an excitation signal, $\mathbf{z}=[\mathbf{y}]$. Like before, a subscript (o, a, b, \dots, u) is used in the signal representation for designating the corresponding state of the structure. The raw experimental signals are usually pre-processed such as low or band-pass filtering, signal down-sampling, etc.

The obtained signals are subsequently analyzed by the AR models. Appropriate models are identified based on data $\mathbf{z}_o, \mathbf{z}_a, \mathbf{z}_b, \dots$ in the baseline phase and based on \mathbf{z}_u in each inspection phase. From each estimated model, the corresponding estimate of a characteristic quantity Q is extracted.

Damage detection is based on a proper comparison of the true Q_u to the true Q_o via a binary statistical hypothesis test as described in the theory section. Damage identification is similarly based on the proper comparison Q_u to each one of Q_a, Q_b, \dots via statistical hypothesis testing procedures (see Tables 1 and 2). Note that the statistical hypothesis test is generally

based on the probabilities of type I and type II errors, or else the false alarm (α) and missed damage (β) probabilities. The method presented in this work is based on the α -level, but when the α -level decreases (increases), β increases (decreases). Figure 1 concisely summarizes the work frame of the damage diagnosis process using the AR models.

In this work, the effectiveness and efficiency of the proposed AR-based damage detection and identification framework in the context of active sensing acousto-ultrasonic guided wave-based SHM are presented over two test cases: an aluminum and a composite plate with simulated damages (weights taped on the surface to simulate damage).

Test case I: aluminum plate with simulated damage

Experimental setup and data acquisition

In this study, to demonstrate ultrasonic guided wave-based damage detection and identification performance in metallic structures using an AR model, an aluminum 6061 coupon with dimension $152.4 \times 279.4 \times 2.36$ mm ($6 \times 11 \times 0.093$ in) was used (Figure 2(a)). The specimen was obtained from the commercial vendor McMaster-Carr. The details of the sensor layout are shown in Figure 2(b). Using Hysol EA 9394 adhesive, six PZT piezoelectric sensors (type PZT-5A, Acellent Technologies, Inc., Sunnyvale, CA, USA) of 6.35 mm ($1/4$ in) diameter and a thickness of 0.2 mm (0.0079 in) were attached to the plate and cured for 24 h in room temperature. Figure 2(b) shows the dimensions of the plate, the placement of the PZT transducers, and the path naming convention. In Figure 2(b), sensors are numbered from 1 through 6. Sensors 1, 2, and 3 are three inches apart from the bottom edge. Similarly, sensors 4, 5, and 6 are three inches apart from the top edge. The distance between the sensor pair (1,4), (2,5), and (3,6) is 5 inches. The distance between the sensor pair (1,2), (2,3), (4,5), and (5,6) is 1.5 inches. When sensor 1 acts as an actuator and sensor 5 acts as a receiver,

Table I. Different structural states, guided wave signals used, and the characteristic quantity for baseline and inspection phases.

Baseline phase			
Structural state	S_o (healthy structure)	S_a (damage type a)	S_b (damage type b)
Guided wave signals	$z_o = (x_o, y_o)$	$z_a = (x_a, y_a)$	$z_b = (x_b, y_b)$
Characteristic quantity	Q_o	Q_a	Q_b
Inspection phase			
Structural state	S_u (current structure in unknown state)		
Guided wave signals	$z_u = (x_u, y_u)$		
Characteristic quantity	Q_u		

Table 2. Statistical hypothesis testing problems for the damage detection and identification tasks.

Damage detection	
$H_0 : Q_u \sim Q_o$	Null hypothesis—healthy structure
$H_1 : Q_u \neq Q_o$	Alternative hypothesis—damaged structure
Damage identification	
$H_A : Q_u \sim Q_a$	Hypothesis a —damage type a
$H_B : Q_u \sim Q_b$	Hypothesis b —damage type b
\vdots	\vdots

the corresponding wave propagation is referred to as path 1–5. Simulated damages were created on the plate by adding small weights to the plate. Each weight was 3 g and up to four 3-g weights were taped to the surface of the plate starting from its center point. In its healthy state of the plate, no weight was added. The number of 3-gram weights attached to the plate corresponds to the level of damage present in the plate. For example, when two weights are added to the plate, it corresponds to damage level 2, and so on. Experimental details for aluminum coupon are summarized in Table 3.

Actuation signals in the form of 5-peak tone bursts (5-cycle Hamming-filtered sine wave, 90 V peak-to-peak, 250 kHz center frequency) were generated in a pitch-catch configuration over each sensor consecutively. Data were collected using a ScanGenie III data

acquisition system (Acellent Technologies, Inc.) from selected sensors during each actuation cycle at a sampling frequency of 24 MHz. 20 signals from each sensor (wave propagation path) and damage state were recorded. This led to a total of 100 data sets (five states, 20 signals per state) for each sensor. For the time-series modeling, the acquired signals were down-sampled to 2 MHz. This process resulted in 612-sample-long signals. Figure 2(c) presents indicative signal realization for different damage (health) states (top subplot) and nonparametric spectrogram of a single signal realization (window length: 30 samples; 98% overlap; Number of discrete Fourier transform points [NFFT] points: 30,000 (zero-padding took place to obtain smooth magnitude estimates); frequency resolution $\Delta f = 666.66$ Hz).

Damage indices

In this work, the following time-domain DI is employed as a reference to compare the performance of the DI-based approach and the time-series model-based approach proposed herein. The DI used here was adopted from the work of Janapati et al.,³ which is characterized by high sensitivity to damage size and orientation and low sensitivity to other variations such as adhesive thickness and the material properties of the structure, sensor locations, etc. Given a baseline signal $y_o[t]$ and an unknown signal $y_u[t]$ indexed with

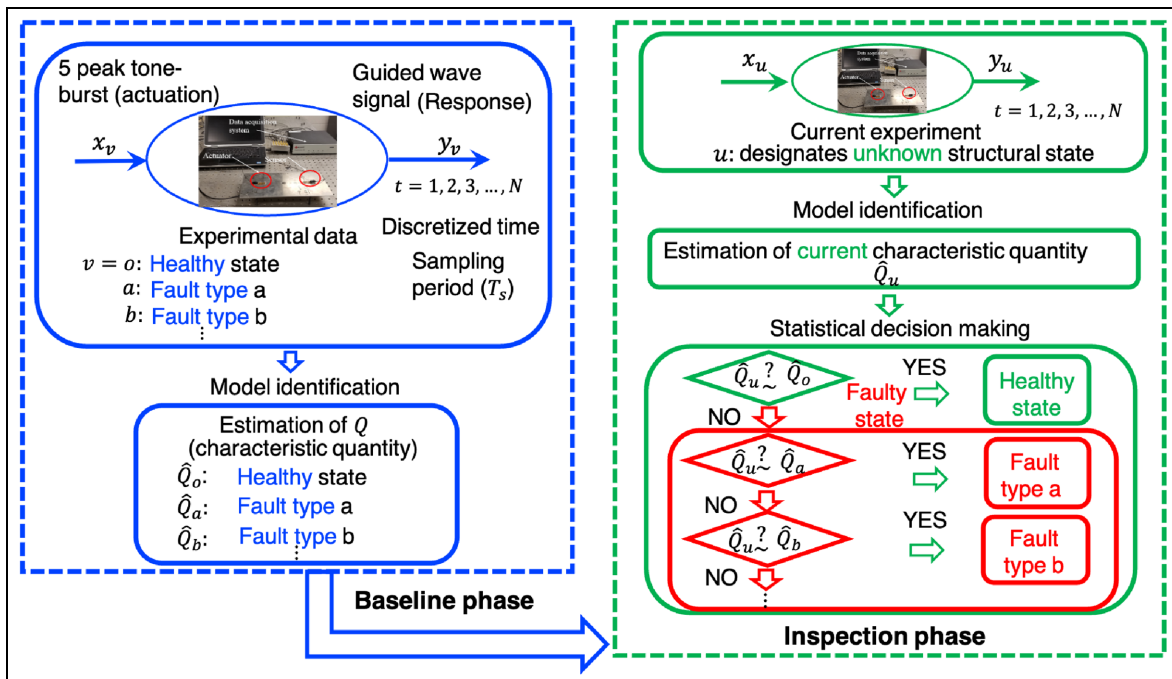


Figure 1. This flow chart summarizes the overall damage diagnosis process. Note that the test statistics obtained in the baseline phase based on the estimated model parameters from the data collected at the structure's healthy state are compared in the inspection phase.

Table 3. Experimental details and data set for the aluminum coupon.

Structural state	Damage level	Number of data sets	Total added weight ^a (g)
Healthy	No damage (healthy)	20	0
1 steel weight	Damage level 1 (dam 1)	20	3
2 steel weight	Damage level 2 (dam 2)	20	6
3 steel weight	Damage level 3 (dam 3)	20	9
4 steel weight	Damage level 4 (dam 4)	20	12

Sampling frequency: $f_s = 24$ MHz. Center frequency range: [150:50:750] kHz. Number of samples per data set $N = 8000$.

^aWeight of tacky tape is not considered.

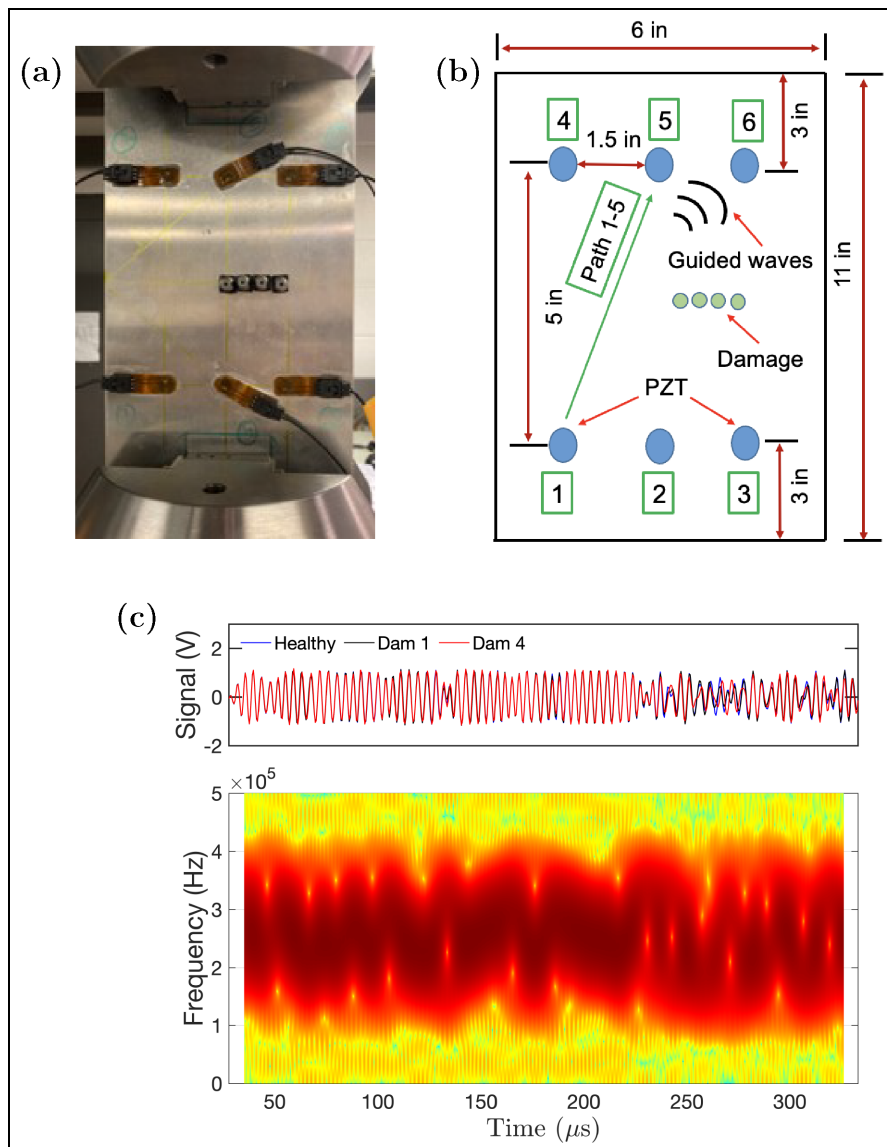


Figure 2. This plot shows the specimen used in the first experiment and a representative ultrasonic signal waveform: (a) the aluminum plate used in this study, (b) a schematic of the plate's sensor layout and dimensions, and (c) the realization of the guided wave signal for healthy and damaged cases with a representative nonparametric spectrogram analysis.

normalized discrete time $t(t=1, 2, 3, \dots, N)$, where N is the number of data samples considered in the calculation of the DI, the formulation of that DI is as follows:

$$Y_u^n[t] = \frac{y_u[t]}{\sqrt{\sum_{t=1}^N y_u^2[t]}} \quad Y_o^n[t] = \frac{y_o[t] \cdot \sum_{t=1}^N (y_o[t] \cdot Y_u^n[t])}{\sum_{t=1}^N y_o^2[t]} \quad (39)$$

$$\text{DI} = \sum_{t=1}^N (Y_u^n[t] - Y_o^n[t])^2 \quad (40)$$

In this notation, $Y_u^n[t]$ and $Y_o^n[t]$ are normalized unknown (inspection) and baseline signals, respectively.

Path selection

In the context of the active sensing guided wave-based SHM, multiple sensors are usually installed at the critical area being monitored, and different actuator sensor paths are used to cross verify the integrity of the component. In the present study, Figure 2(b) shows the actuator-sensor layout where six sensors/actuators were used. In this study, simulated damages were used in the form of weights mounted to the plate with tacky tapes. The weights started from the center of the plate and grew in magnitude to the right. It was shown that when the guided wave signal crosses the damage (known as the damage-intersecting path), a significant change can be observed in the signal with the increase in the damage size. However, this was not the case for a damage non-intersecting path. The received signals sustain significantly smaller changes with the increase

in damage size. In this work, one state-of-the-art DI from the literature was explored to see how damage intersection affects damage detection using the DI approach. Figure 3(a) and (b) show the evolution of the DI with increasing damage size for a damage non-intersecting and intersecting path, respectively. It can be observed that the magnitude of the DI for the damage non-intersecting path is much smaller than the damage intersecting path. As a result, damage detection and identification are challenging using a damage non-intersecting path. In the subsequent study, it is shown that using an AR model, perfect damage detection and identification are possible even for damage non-intersecting paths.

Parametric identification and damage detection results

To detect and identify damage using an AR model, it is first necessary to identify the system in its healthy state for each path while the guided wave signals are being propagated. Figure 4 shows the AR model identification process of the aluminum plate in its healthy state for damage intersecting path 2–6. The identification of the damage non-intersecting path 1–4 provides similar results as that of Figure 4. For the sake of brevity, it has not been shown here.

Model selection of AR models can be performed by selecting the appropriate model order n_a . The RSS/SSS criterion was employed for the model selection process. It describes the predictive ability of the model. AR orders from $n_a = 2$ to $n_a = 15$ were considered. It should be mentioned here that as stationary AR models are

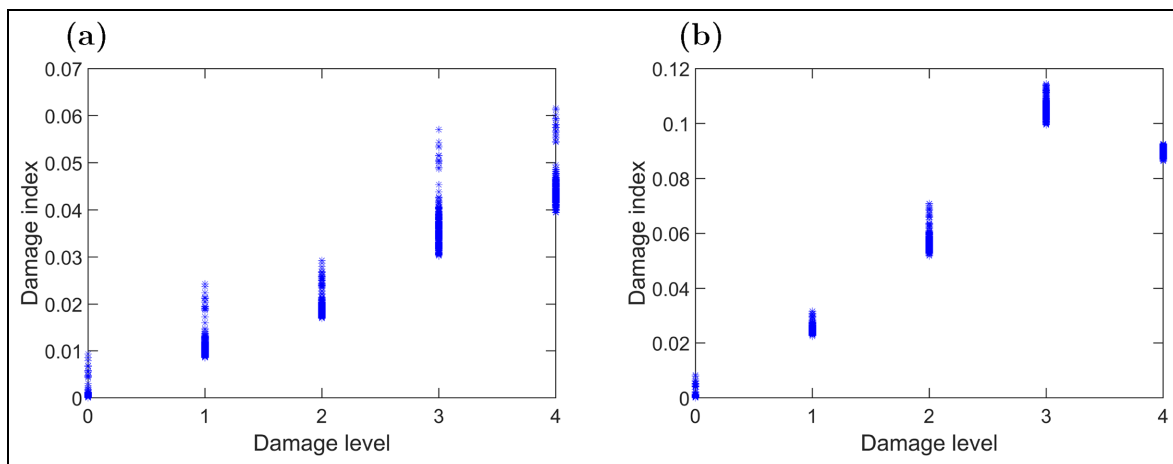


Figure 3. The evolution of the damage index as applied to indicative actuator-sensor paths: (a) damage non-intersecting path 1–4 and (b) damage intersecting path 2–6. Note that the magnitude of the damage index increases with increasing damage level for damage non-intersecting path 1–4, although overlap of damage indices occurs between different damage levels. For damage intersecting path 2–6, the increase in damage index with damage level is not monotonic.

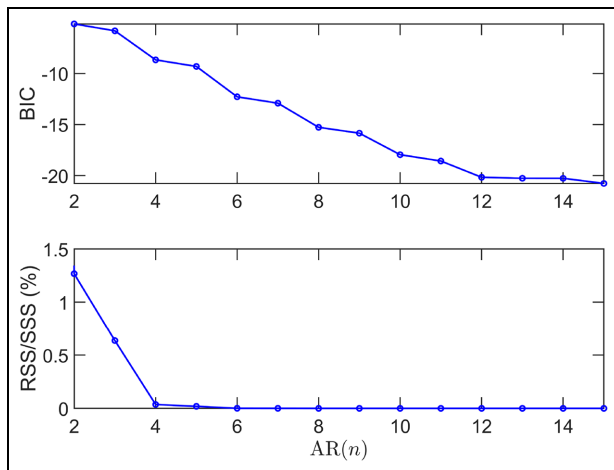


Figure 4. Model order selection via the BIC (top) and RSS/SSS (bottom) criteria for damage intersecting path 2–6. Note that the BIC criterion suggests the use of model order $na = 12$; however, the RSS/SSS criterion suggests $na = 4$.

BIC: Bayesian information criterion; RSS: residual sum of squares; SSS: signal sum of squares.

being used to model a nonstationary response signal, perfect white residuals are not expected with an arbitrarily large model order keeping a reasonable sample per parameter value. Hence, model orders greater than $na = 15$ are not considered. Among all these models, the best model was chosen where the RSS/SSS values start to show a plateau. Following this criterion, the best model occurred for $na = 4$. In addition to the RSS/SSS criterion, the BIC, which rewards the model's predictive capability while penalizing model complexity for increasing model order, was also taken into account (Figure 4). Model validation took place via examination of the whiteness, or uncorrelatedness, and normality hypothesis of the model residuals.

It is to be mentioned here that for the estimation of the model parameters, an asymptotically efficient WLS estimator was employed in this study. The use of a different estimator may provide a slightly different parameter estimate, which may subsequently affect the damage diagnosis process.

Figure 5(a) and (b) depicts the AR model parameters for damage intersecting path 2–6 and damage non-intersecting path 1–4, respectively, for all different structural states, namely, healthy, damage level 1, damage level 2, damage level 3, and damage level 4. For each state, 20 realizations are considered. The solid lines represent the mean parameter values, and the shaded regions represent the ± 2 standard deviation confidence intervals derived from the 20 realizations. As the model order $na = 4$, the number of estimated parameters is also four. Note that the parameters of the damage intersecting path 2–6 for different

structural states are well separated and the confidence intervals are also narrower compared to the damage non-intersecting path 1–4. However, an exception occurred for the parameter α_4 , where different structural states overlapped. Figure 6(a) and (b) show the evolution of parameter α_1 for different structural states for damage intersecting path 2–6 and damage non-intersecting path 1–4, respectively. The black lines represent the mean parameter values, and the green regions represent the 95% confidence intervals. It can be observed that for damage intersecting path 2–6, different states are well separated and the confidence intervals also do not overlap. However, for damage non-intersecting path 1–4, the confidence bound for damage level 1 overlaps with the healthy case, and the confidence bound for damage levels 2 and 3 overlaps with each other.

For damage detection, all four parameters may not be needed or may be redundant in some cases. The use of all the parameters may reduce the damage detection performance when model parameters are correlated. As described in the theoretical section, three approaches have been taken in this regard. The first one is the standard one, where all the model parameters are used. The second one is referred to as the SVD-based approach, and the third one is known as the PCA-based approach. Figure 7 shows the parameter selection process for damage detection and identification in an aluminum plate for damage intersecting path 2–6. From Figure 7(a), it can be observed that the eigenvalues λ_1 and λ_4 have the highest magnitude. As a result, the corresponding parameters α_1 and α_4 were used for the subsequent damage detection and identification using the SVD-based approach. From Figure 7(b), it can be observed that after projecting the parameters onto some lower dimensional space, only two parameters are needed for explaining the total variance. As a result, the truncated parameters and the associated covariance matrix were used for the subsequent damage detection and identification using the PCA-based approach. Similar results were obtained for the damage non-intersecting path 1–4, and for the sake of brevity, those are not shown.

Figure 8 shows the correlation between the model parameters. Figure 8(a) shows the plot of parameters α_1 and α_2 for damage non-intersecting path 1–4 and notice that they are highly correlated. Including highly correlated parameters in the damage detection algorithm reduces the performance of the damage detection process. Figure 8(b) shows a three-dimensional view of parameter α_1 , α_2 , and α_4 . Figure 8(c) shows the correlation between α_1 and α_4 . Notice that the parameters are not correlated and different damage states are separated. Also, note from Figure 7(a) that the eigenvalues of the corresponding parameters α_1 and α_4 have the

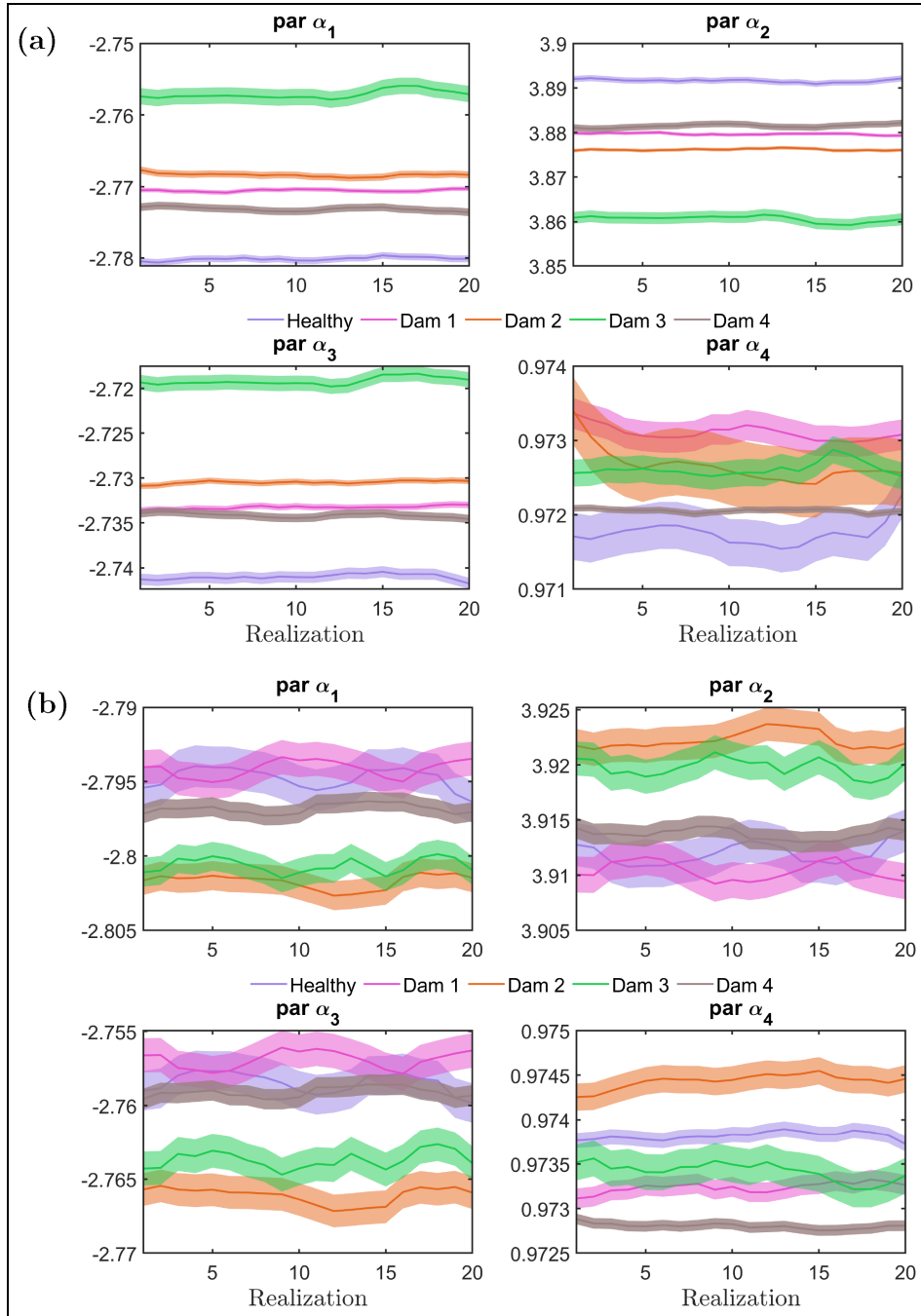


Figure 5. AR(4)-based model parameters for different structural states: the parameter mean is shown as solid lines and the associated ± 2 standard deviation is shown as shaded regions: (a) damage intersecting path 2–6 and (b) damage non-intersecting path 1–4. Note that the parameters of damage intersecting path 2–6 are relatively separated compared to the damage non-intersecting path 1–4, which makes damage detection easier for damage intersecting paths in metallic structures. AR: autoregressive.

highest magnitude which suggests the use of the parameters α_1 and α_4 in the damage diagnosis process. Figure 8(d) shows that after performing PCA, the model parameters become more uncorrelated and separated for different structural states.

Figure 9 shows the damage detection performance of the damage intersecting path 2–6 using the standard AR, SVD, and PCA-based approaches. In this case, the covariance matrix was derived from the 20 experimental healthy signals. It can be observed that for all

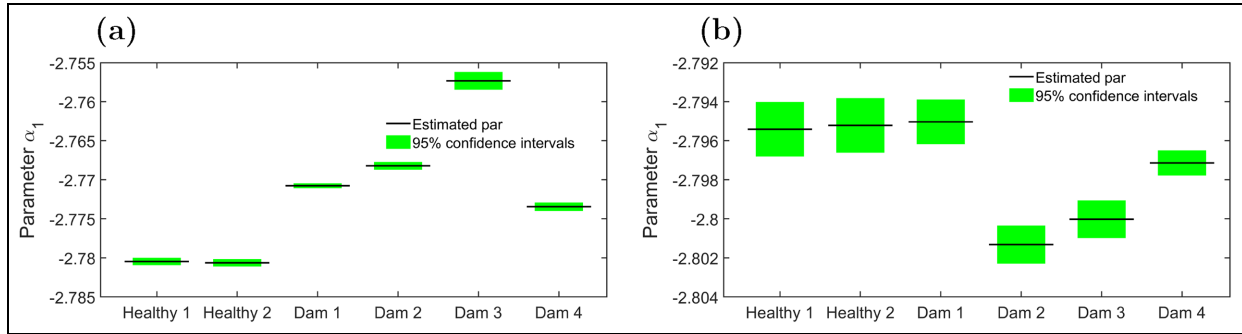


Figure 6. Estimated model parameters for healthy and damaged states and the corresponding 95% confidence intervals: (a) parameter α_1 for damage intersecting path 2–6 and (b) parameter α_1 for damage non-intersecting path 1–4. Note that for the damage intersecting path 2–6, the confidence interval of the parameter α_1 is less overlapped among different damage levels compared to the damage non-intersecting path 1–4.
AR: autoregressive.

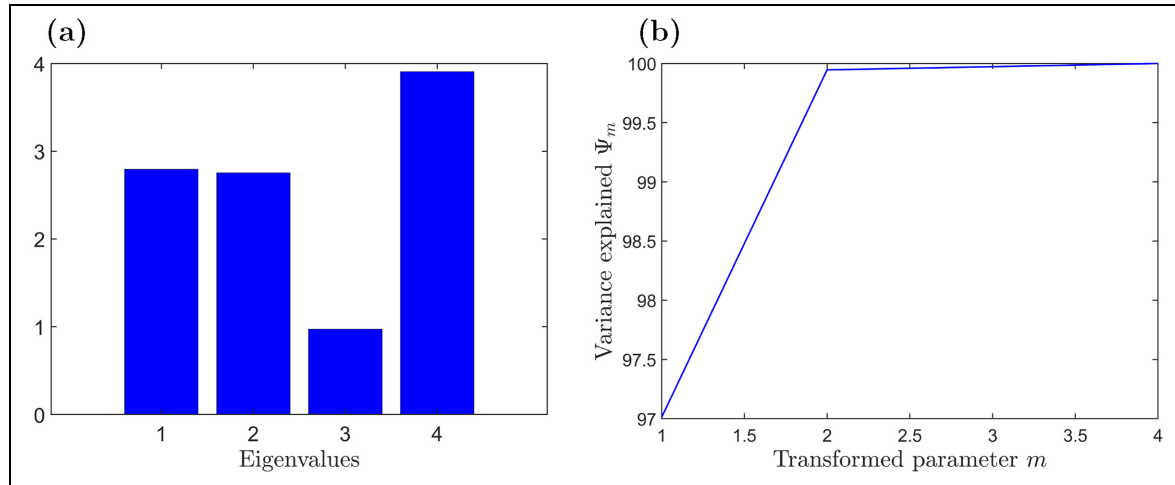


Figure 7. AR parameter selection process for damage detection and identification of the damage intersecting path 2–6: (a) SVD-based approach and (b) PCA-based approach. Note that the PCA-based approach suggests the use of only two parameters.
AR: autoregressive; SVD: singular value decomposition; PCA: principal component analysis.

three cases, perfect damage detection was achieved. The α -level used for the standard AR and SVD-based approaches was 1×10^{-9} . For the PCA-based approach, the threshold was manually adjusted as the α -level exceeds the numerical limit. Similarly, Figure 10 shows the damage detection using the above-mentioned three methods using the covariance matrix derived from the AR(4) model. It can be observed that for the standard AR and SVD-based methods, perfect damage detection was achieved. However, for the PCA-based approach, damage level 4 goes inside the threshold. For all three cases, the thresholds were manually adjusted as the α -level goes close to 1 when using AR(4)-based covariance.

Figure 11 shows the damage detection performance of the damage non-intersecting path 1–4 using the

standard AR, SVD, and PCA-based approaches. In this case, the covariance matrix was derived from the 20 experimental healthy signals. It can be observed that perfect damage detection was achieved for all three cases when experimental covariance was used. The α -level used for the standard AR and SVD-based approaches was 1×10^{-9} . For the PCA-based approach, the threshold was manually adjusted.

When using the AR(4)-based covariance matrix, the performance of standard AR and SVD-based method was bad as the damage level 1 was missed (Figure 12(a) and (b)). However, the PCA-based approach perfectly detects damage when the AR(4)-based covariance was used (Figure 12(c)). For all three cases, the thresholds were manually adjusted as the α -level exceeded the numerical limit when using AR(4)-based covariance.

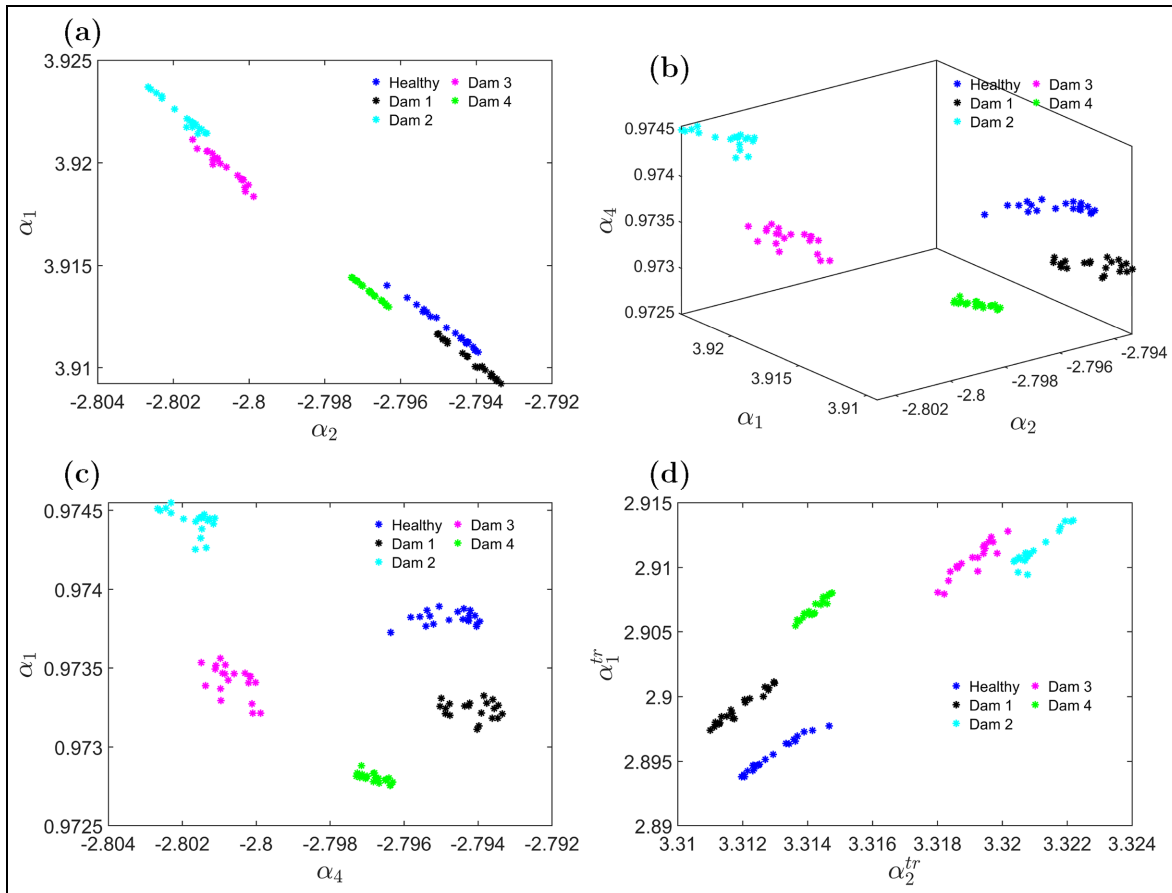


Figure 8. Indicative AR(4) model parameters are shown for damage non-intersecting path I–4: (a) model parameters α_1 and α_2 , (b) model parameters α_1 , α_2 , and α_4 , (c) model parameters to be used in the damage diagnosis process indicated by the SVD approach (α_1 and α_4), and (d) truncated model parameters from PCA transformation. Note that the model parameters of different structural states are nicely separated after PCA and SVD transformation.

AR: autoregressive; SVD: singular value decomposition; PCA: principal component analysis.

Table 4 compactly summarizes the α -level used for the aluminum plate.

Figure 13 shows the damage identification results for the damage intersecting path 2–6 for the aluminum plate using the experimental covariance matrix. It can be observed that perfect damage identification was achieved with no missed classification. Table 5 compactly summarizes the damage detection and identification results for the standard AR, SVD, and PCA-based methods for the two indicative paths and the associated covariance matrix used. It can be observed that, for the aluminum plate, perfect damage detection and identification is possible both for damage intersecting and non-intersecting paths when the experimental covariance matrix is used.

The proper selection of the risk level α (type I error) is of crucial importance as it is associated with the methods' robustness and effectiveness. If the α -level is not properly adjusted, damage diagnosis will be

ineffective, as false alarms, missed damage, and damage misclassification cases may occur. To take into account this issue, receiver operating characteristics (ROC) curves can be plotted, which investigates the relationship between the false positive rate and true positive rate for different α -levels. ROC plots may provide insight into the methods' robustness and effectiveness.

Figure 14 shows the ROC plots of the SVD-based method for the damage non-intersecting path 1–4 and the damage intersecting path 2–6 using the experimental as well as the theoretical covariance matrix. In constructing each plot, the threshold of the Q -statistics was varied from -100 to 10^5 with an increment of 1, that is, covering all possible values. The best possible method for damage detection would pass through a point in the upper left corner with a coordinate $(0,1)$ in the ROC space. This point represents 100% sensitivity, that is, no false negative, and 100% specificity, that is,

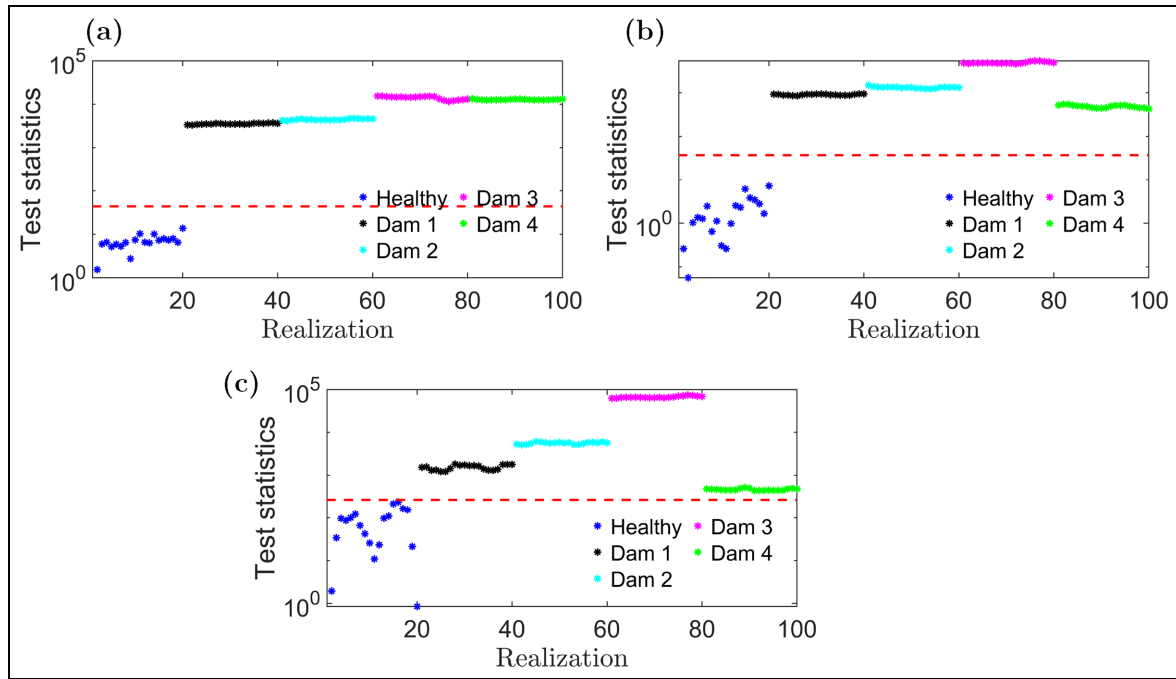


Figure 9. Damage detection performance comparison for damage intersecting path 2–6 using the covariance matrix derived from 20 experimental healthy signals: (a) standard AR approach, (b) SVD-based approach, and (c) PCA-based approach. Note that for damage intersecting path 2–6 and the experimental covariance matrix, all three approaches show good performance.
AR: autoregressive; SVD: singular value decomposition; PCA: principal component analysis.

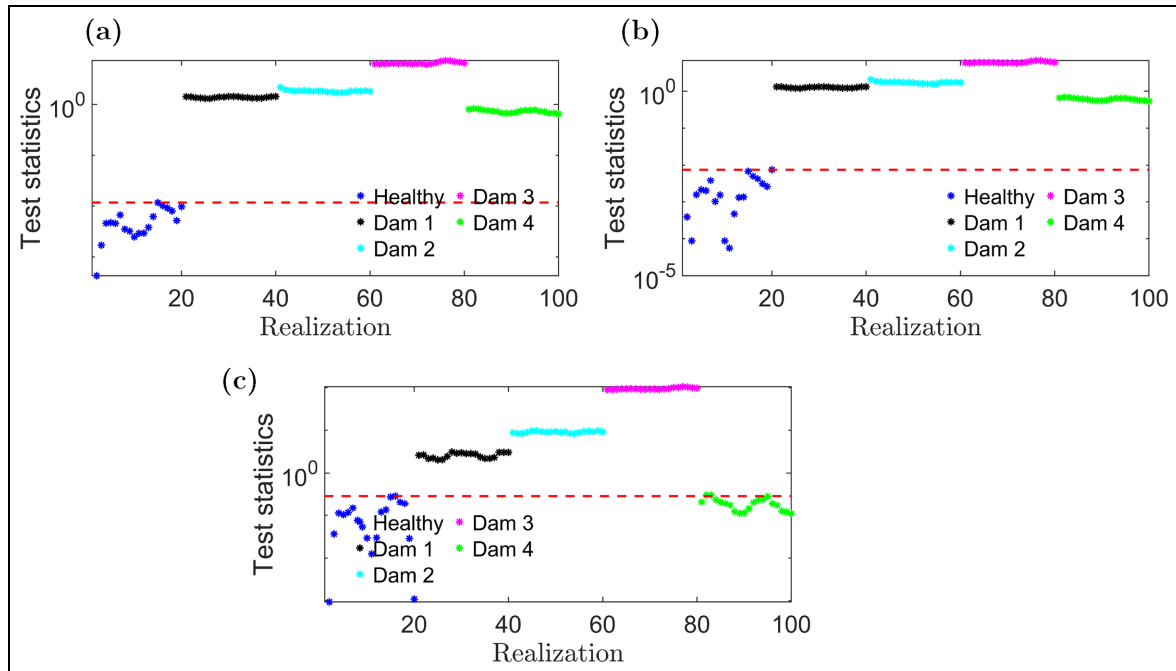


Figure 10. Damage detection performance comparison for damage intersecting path 2–6 using the AR(4)-based covariance matrix: (a) standard AR approach, (b) SVD-based approach, and (c) PCA-based approach. Note that for damage intersecting path 2–6 and AR(4)-based covariance matrix, only standard AR and SVD-based approaches show good performance.
AR: autoregressive; SVD: singular value decomposition; PCA: principal component analysis.

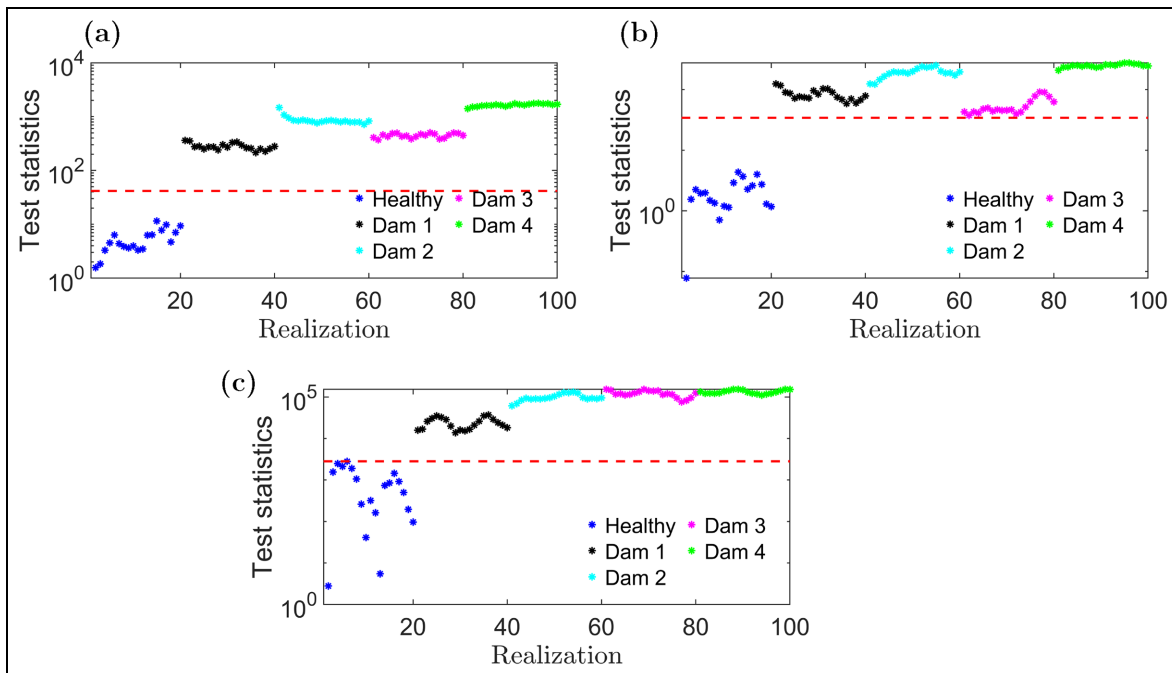


Figure 11. Damage detection performance comparison for damage non-intersecting path 1–4 using the covariance matrix derived from 20 experimental healthy signals: (a) standard AR approach, (b) SVD-based approach, and (c) PCA-based approach. Note that for damage non-intersecting path 1–4 and experimental covariance matrix, all three methods show good performance.
AR: autoregressive; SVD: singular value decomposition; PCA: principal component analysis.

Table 4. The α -level chart for the aluminum plate.

Method	Path	Covariance	α -level
Standard AR	1–4	Experiment	1×10^{-9}
	1–4	Theory	Manual
	2–6	Experiment	1×10^{-9}
	2–6	Theory	Manual
SVD-based	1–4	Experiment	1×10^{-9}
	1–4	Theory	Manual
	2–6	Experiment	1×10^{-9}
	2–6	Theory	Manual
PCA-based	1–4	Experiment	Manual
	1–4	Theory	Manual
	2–6	Experiment	Manual
	2–6	Theory	Manual

AR: autoregressive; SVD: singular value decomposition; PCA: principal component analysis.

no false positives. As such, this point is called perfect classification. A random guess would provide a point along the diagonal line. This line is referred to as the point of no discrimination. Methods that generate points below this line are bad predictors or classifiers. In Figure 14(a), (c), and (d), the red line passes through the point (0,1) which means perfect detection capability has been achieved. In addition, in Figure 14(b), the red line does not pass through the point (0,1). As such,

when using AR(4)-based covariance, the method may not show perfect detection capability for the aluminum plate.

Test case II: CFRP plate with simulated damage

Experimental setup and data acquisition

The second experimental setup consists of a carbon fiber reinforced plastic (CFRP) coupon with a dimension of $152.4 \times 254 \times 2.36$ mm ($6 \times 10 \times 0.093$ in). The coupons were acquired from (ACP Composites, Inc., Livermore, CA, USA) which had $0/90^\circ$ unidirectional layup with Carbon fiber prepreg. Similar to the case of the aluminum coupon, the CFRP coupon was also fitted with six PZT sensors (PZT-5A) using Hysol EA 9394 adhesive. To simulate damage, up to six 3-g weights were sequentially attached to the surface of the plate using tacky tape as shown in Figure 15(a). Data acquisition and analysis were done in the same manner as in the case of the aluminum coupon. Experimental details for the composite coupon are summarized in Table 6.

Path selection

In the present study, Figure 15(a) shows the six sensors/actuators layout in the CFRP plate. Simulated

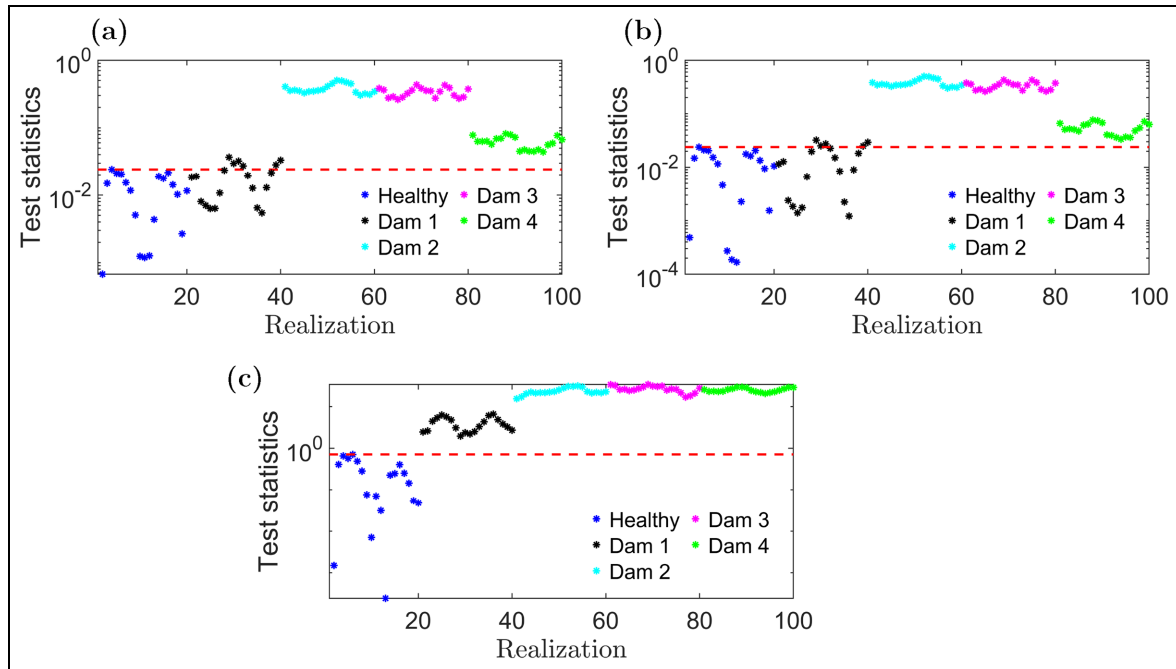


Figure 12. Damage detection performance comparison for damage non-intersecting path 1–4 using the AR(4)-based covariance matrix: (a) standard AR approach, (b) SVD-based approach, and (c) PCA-based approach. Note that for damage non-intersecting path 1–4 and AR(4)-based covariance matrix, only the PCA-based method performs well.

AR: autoregressive; SVD: singular value decomposition; PCA: principal component analysis.

damage starts from just below sensor 5 and increases in magnitude toward sensor 2. Figure 16(a) and (b) show the evolution of the DI with increasing damage size for damage non-intersecting path 1–4 and damage intersecting path 3–4, respectively. Notice that the magnitude of the DI for the damage non-intersecting path is smaller than the damage intersecting path. However, a higher degree of overlap of the DIs among different damage levels for different realizations exists for the damage intersecting path 3–4 than the damage non-intersecting path 1–4. As a result, damage detection and identification are challenging using the damage intersecting path 3–4 for the CFRP coupon, although the magnitude of the DIs is higher for damage intersecting path 3–4. In the subsequent study, it is shown that using an AR model, perfect damage detection was achieved for the CFRP coupon, however, perfect damage identification remains challenging using the stationary time-series models.

Parametric identification and damage detection results

Similar to the case of the aluminum plate, for composites, the RSS/SSS criterion, describing the predictive ability of the model, was employed for the model selection process. AR orders from $na=2$ to $na=15$ were

considered to create a pool of candidate models. Among all these models, the best model can be chosen where the RSS/SSS values start to show a plateau. Following this criterion, from Figure 17, it can be observed that for $na=4$, the plateau starts to occur (both for damage intersecting and non-intersecting paths). However, selecting the model order $na=4$ results in highly correlated model parameters, and the model parameters of different damage states overlap. As a result, $na=6$ was selected as the final model order for damage detection and identification in the CFRP plate.

Figure 18(a) and (b) depict the mean AR model parameters and the associated ± 2 standard deviation confidence intervals for all different structural states, namely, healthy, damage level 1, damage level 2, damage level 3, damage level 4, damage level 5, and damage level 6 for the damage intersecting path 3–4 and the damage non-intersecting path 1–4 of the CFRP plate, respectively. For each state, 20 realizations of the guided wave signals are considered. The solid lines represent the mean parameter values, and the shaded regions represent the ± 2 standard deviation confidence intervals. As the model order $na=6$, the number of estimated parameters is also six. Note that the model parameters of different states overlap both for damage intersecting and non-intersecting paths (as opposed to

Table 5. Damage detection and identification summary results for the aluminum plate.

Method	Path	Covariance	Damage detection				
			False alarms	Missed damage			
				Healthy	Damage 1	Damage 2	Damage 3
Standard AR	1–4	Experiment	0/20	0/20	0/20	0/20	0/20
	1–4	Theory	0/20	14/20	0/20	0/20	0/20
	2–6	Experiment	0/20	0/20	0/20	0/20	0/20
	2–6	Theory	0/20	0/20	0/20	0/20	0/20
SVD based	1–4	Experiment	0/20	0/20	0/20	0/20	0/20
	1–4	Theory	0/20	15/20	0/20	0/20	0/20
	2–6	Experiment	0/20	0/20	0/20	0/20	0/20
	2–6	Theory	0/20	0/20	0/20	0/20	0/20
PCA based	1–4	Experiment	0/20	0/20	0/20	0/20	0/20
	1–4	Theory	0/20	0/20	0/20	0/20	0/20
	2–6	Experiment	0/20	0/20	0/20	0/20	0/20
	2–6	Theory	0/20	0/20	0/20	0/20	20/20
Damage identification							
Method	Path	Covariance	Damage misclassification				
			Damage 1	Damage 2	Damage 3	Damage 4	
Standard AR	1–4	Experiment	(-,0,0,0)	(0,-,0,0)	(0,0,-,0)	(0,0,0,-)	
	1–4	Theory	(-,0,0,0)	(0,-,13,0)	(0,20,-,0)	(0,0,0,-)	
	2–6	Experiment	(-,0,0,0)	(0,-,0,0)	(0,0,-,0)	(0,0,0,-)	
	2–6	Theory	(-,0,0,0)	(0,-,0,0)	(0,0,-,0)	(0,0,0,-)	
SVD based	1–4	Experiment	(-,0,0,0)	(0,-,0,0)	(0,0,-,0)	(0,0,0,-)	
	1–4	Theory	(-,0,0,0)	(0,-,12,0)	(0,18,-,0)	(0,0,0,-)	
	2–6	Experiment	(-,0,0,0)	(0,-,0,0)	(0,0,-,0)	(0,0,0,-)	
	2–6	Theory	(-,0,0,0)	(0,-,0,0)	(0,0,-,0)	(0,0,0,-)	
PCA based	1–4	Experiment	(-,0,0,0)	(14,-,13,11)	(0,18,-,20)	(0,5,16,-)	
	1–4	Theory	(-,0,0,0)	(5,-,17,20)	(0,19,-,20)	(0,14,13,-)	
	2–6	Experiment	(-,0,0,0)	(0,-,0,0)	(0,0,-,0)	(0,0,0,-)	
	2–6	Theory	(-,0,0,0)	(0,-,0,0)	(0,0,-,0)	(0,0,0,-)	

AR: autoregressive; SVD: singular value decomposition; PCA: principal component analysis.

aluminum plate). For parameter α_6 , the degree of overlapping is higher for the damage intersecting path 3–4 than the damage non-intersecting path 1–4 for different structural states.

Figure 19(a) and (b) shows the evolution of parameter α_1 for different structural states for damage intersecting path 3–4 and damage non-intersecting path 1–4, respectively. The black lines represent the mean parameter values, and the green regions represent the 95% confidence intervals. It can be observed that both for damage intersecting path 3–4 and damage non-intersecting path 1–4, a certain degree of overlap exists among different structural states of the CFRP plate. This is one reason that makes damage detection and identification in the CFRP plate more challenging.

Figure 20 shows the parameter selection process for damage detection and identification in the CFRP plate. From Figure 20(a), it can be observed that the eigenvalues λ_1 and λ_6 have the highest magnitude. As a result,

the corresponding parameters α_1 and α_6 are required to be chosen. However, using only these two parameters, perfect damage detection cannot be achieved in the CFRP plate. Other parameters such as α_2 , α_3 , and α_5 are also required to be included for better damage detection and identification. This may be due to the fact that the wave propagation in CFRP coupon is more complex and the stationary AR models may not be able to capture some of the distinguishing features of the damage embedded in the signals. From Figure 20(b), it can be observed that after projecting the parameters onto some lower dimensional space, only two parameters are needed for explaining the total variance. However, using only two truncated parameters cannot achieve perfect damage diagnosis in the CFRP plate. As a result, five truncated parameters and the associated covariance matrix were used for the subsequent damage detection and identification using the PCA-based approach.

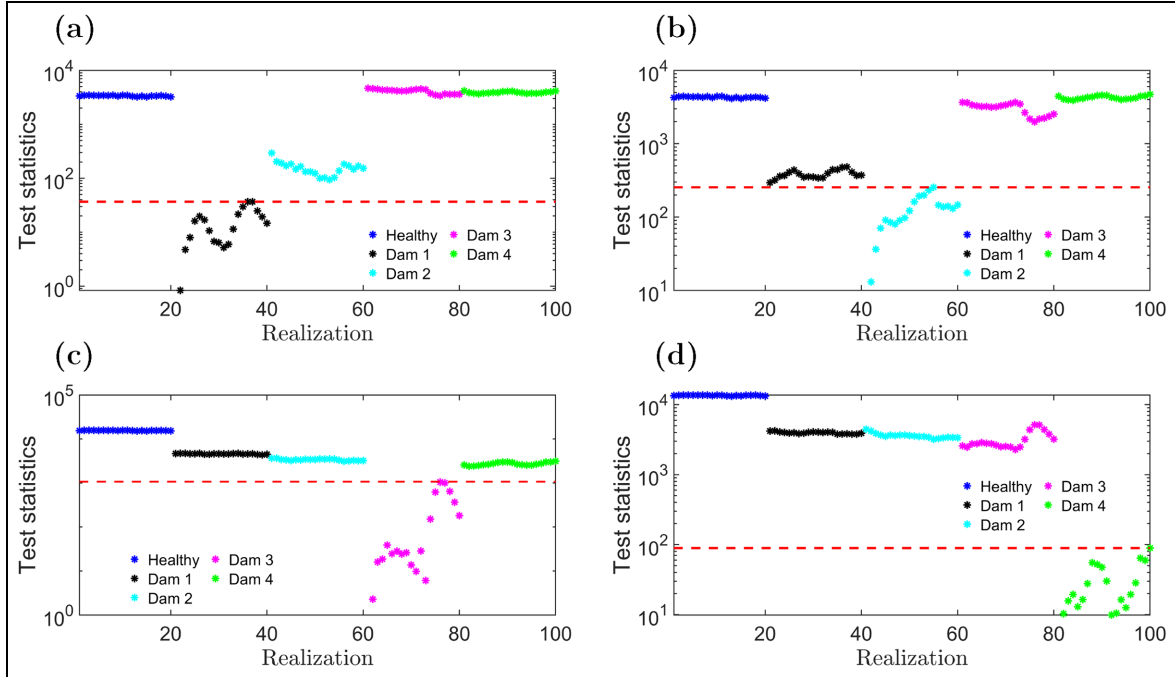


Figure 13. Damage identification results for the damage intersecting path 2–6 using the standard AR approach and using experimental covariance: (a) damage level 1, (b) damage level 2, (c) damage level 3, and (d) damage level 4. Note that only the respective damage level that is being identified remains below the threshold, and all other structural states remain outside the threshold. That is, perfect damage identification has been achieved.

Figure 21(a) shows the plot of the two parameters α_1 and α_2 for all structural states for damage non-intersecting path 1–4. Note that the parameters are highly correlated and different structural states overlap with each other. Figure 21(b) shows a three-dimensional plot of the three model parameters α_1 , α_2 , and α_6 . Figure 21(c) shows the plot of the two parameters α_1 and α_6 . Note that, similar to the case of the aluminum plate, the parameters are less correlated and different structural states are slightly separated. Figure 21(d) shows that after performing PCA transformation, the model parameters become uncorrelated and separated for different structural states.

Figure 22 shows the damage detection performance of the CFRP plate for damage intersecting path 3–4 using the standard AR, SVD, and PCA-based approaches. In this case, the covariance matrix was derived from the 20 experimental healthy signals. It can be observed that for the CFRP plate, the standard AR and the SVD-based approaches perform better than the PCA-based approach. The PCA-based approach shows poor performance in this case. Both for SVD and PCA-based approaches, five parameters were used. Note that for the standard AR and the SVD-based approaches, there is no missed damage. However, for the PCA-based approach, there are instances of missed damage for different damage levels.

The α -level used for the standard AR and SVD-based approaches was 1×10^{-9} . It was manually adjusted for the PCA-based approach as the α -level exceeded the numerical limit. Similarly, Figure 23 shows the damage detection using the above-mentioned three methods using the covariance matrix derived from the AR(6) model. Note that for the standard AR and SVD-based approaches, perfect damage detection was achieved; however, for the PCA-based approach, there are presence of missed damage. The thresholds were manually adjusted for the standard AR and SVD-based approaches. The α -level used for the PCA-based approach was 0.09.

Figure 24 shows the damage detection performance of the damage non-intersecting path 1–4 using the standard AR, SVD, and PCA-based approaches. In this case, the covariance matrix was derived from the 20 experimental healthy signals. It can be observed that, for the case of the CFRP plate, perfect damage detection (all damage states) was achieved for the damage non-intersecting path 1–4 for the standard AR, SVD, and PCA-based approaches. The α -level used for the standard AR and SVD-based case was 1×10^{-10} . For the PCA-based case, the α -level was manually adjusted as it exceeded the numerical limit. Figure 25(a) to (c) show the damage detection performance of the damage non-intersecting path 1–4 using the

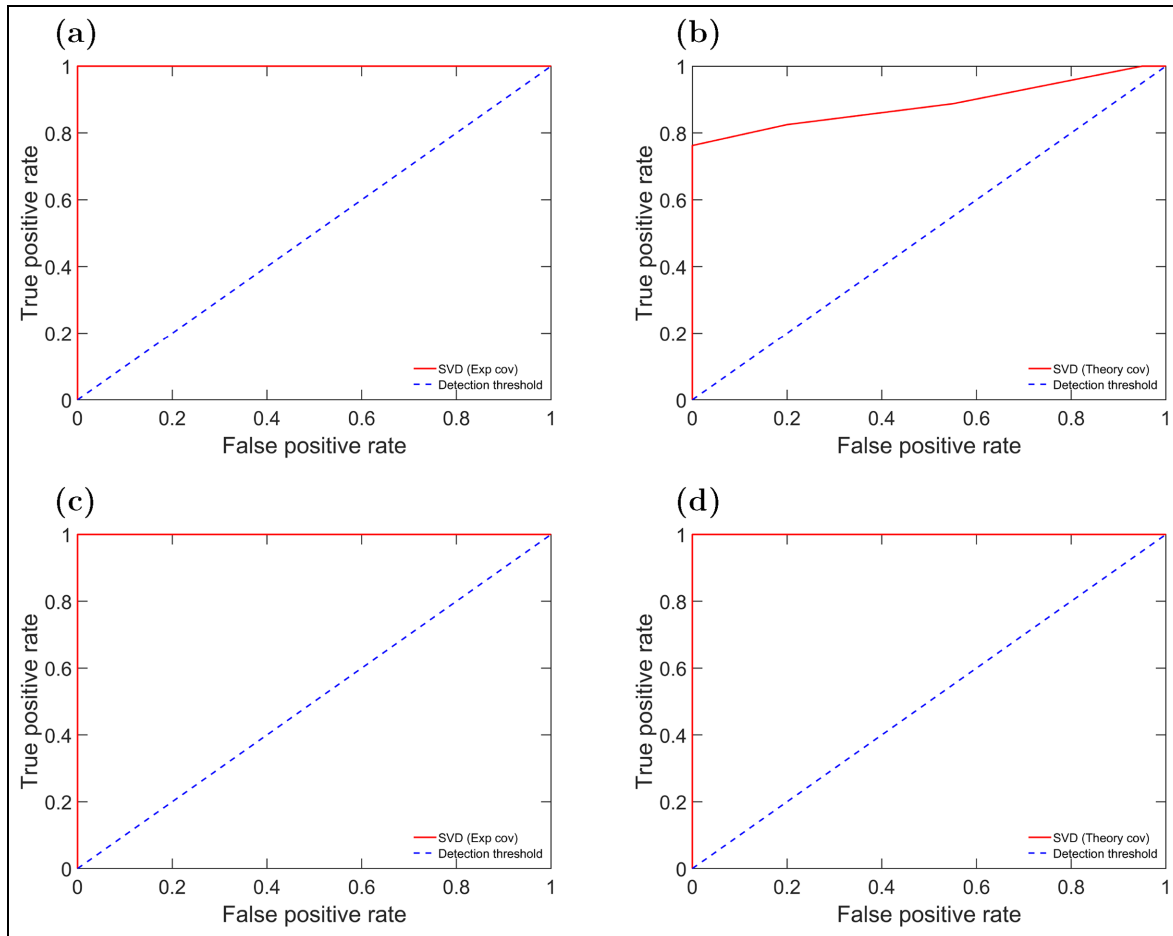


Figure 14. ROC plots comparing the SVD-based damage detection methods for the aluminum plate for different paths and covariance used: (a) path 1–4 with the experimental covariance, (b) path 1–4 with the AR(4)-based covariance, (c) path 2–6 with the experimental covariance, and (d) path 2–6 with the AR(4)-based covariance. The dotted diagonal line represents the discrimination threshold. The red line represents the damage detection capability of the method and perfect detection was achieved for (a), (c), and (d), as the red line passes through the point (0,1), the point of perfect classification.

AR: autoregressive; SVD: singular value decomposition; ROC: receiver operating characteristic.

Table 6. Experimental details and data set for the CFRP coupon.

Structural state	Damage level	Number of data sets	Total added weight ^a (g)
Healthy	No damage (healthy)	20	0
1 steel weight	Damage level 1 (dam 1)	20	3
2 steel weight	Damage level 2 (dam 2)	20	6
3 steel weight	Damage level 3 (dam 3)	20	9
4 steel weight	Damage level 4 (dam 4)	20	12
5 steel weight	Damage level 5 (dam 5)	20	15
6 steel weight	Damage level 6 (dam 6)	20	18

CFRP: carbon fiber reinforced plastic.

Sampling frequency: $f_s = 24$ MHz. Center frequency range: [150:50:750] kHz. Number of samples per data set $N = 8000$.

^aWeight of tacky tape is not considered.

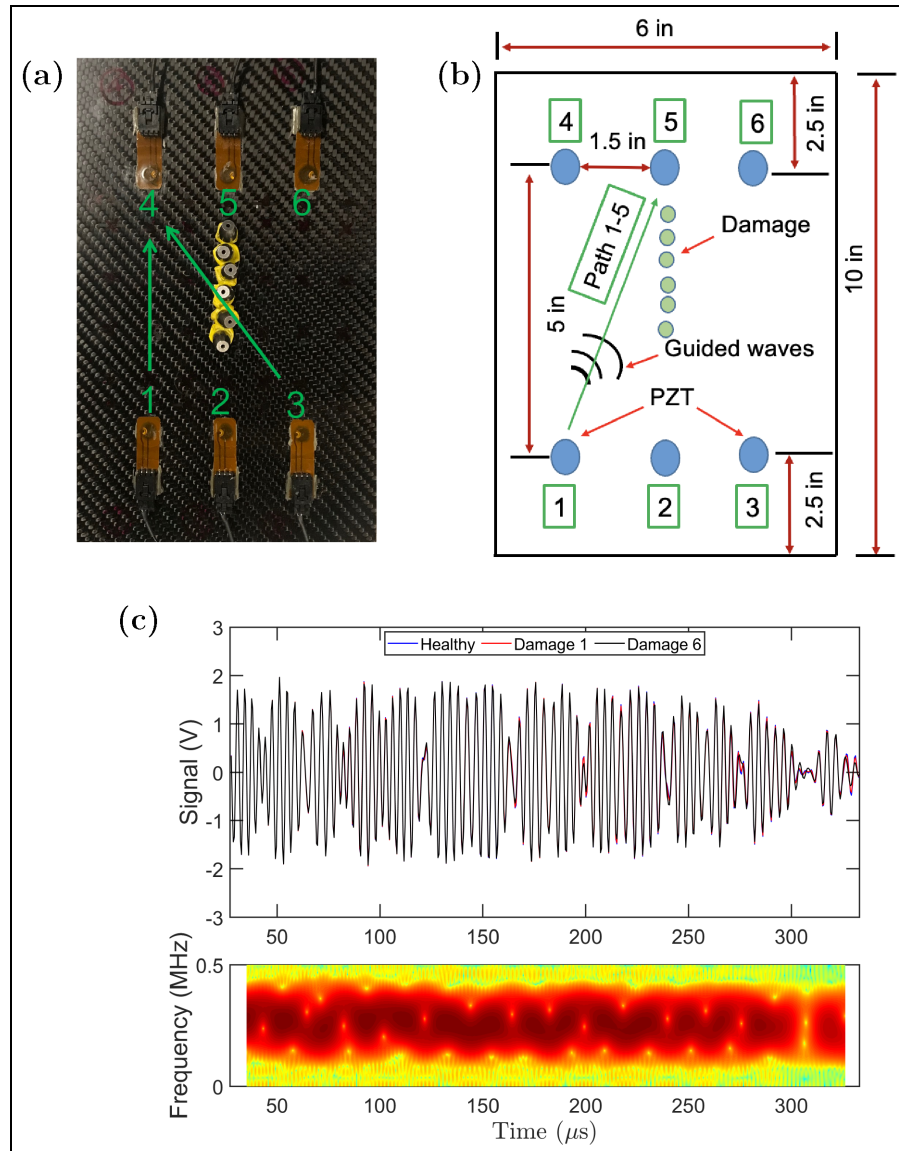


Figure 15. (a) The CFRP plate used in this study fitted with the PZT sensors, (b) the detailed layout of the sensor positions and damage locations as well as the CFRP plate dimensions, and (c) realization of the guided wave signal for healthy and damaged cases with a representative nonparametric spectrogram analysis. Note that in the waveform signal, the distinction between the S_0 or A_0 mode is not evident, and the signal amplitude diminishes after 300 μ s.

CFRP: carbon fiber reinforced plastic; PZT: lead zirconate titanate.

standard AR, SVD, and PCA-based approaches using the AR(6)-based covariance. It can be observed that perfect detection was achieved for all three cases. The thresholds were manually adjusted when using AR(6)-based covariance as the α -level goes close to 1. Table 7 compactly shows the different α -level used in the composite coupon study.

Figure 26 shows the damage identification results for the damage non-intersecting path 1–4 for the CFRP plate using the standard AR-based approach and using the covariance matrix derived from 20 experimental healthy signals. It can be observed that

all the damage levels were perfectly identified with no missed classification.

Figures 27 shows the ROC curves of the SVD-based method for the damage non-intersecting path 1–4 and the damage intersecting path 3–4 using the experimental as well as the theoretical covariance matrix. In constructing each plot, the threshold of the Q -statistics was varied from -100 to 10^5 with an increment of 1, that is covering all possible values. Similar to the case of aluminum plate, the dotted blue lines along the diagonal in Figure 27 represent the point of no discrimination, that is, the sensitivity and specificity values provided by

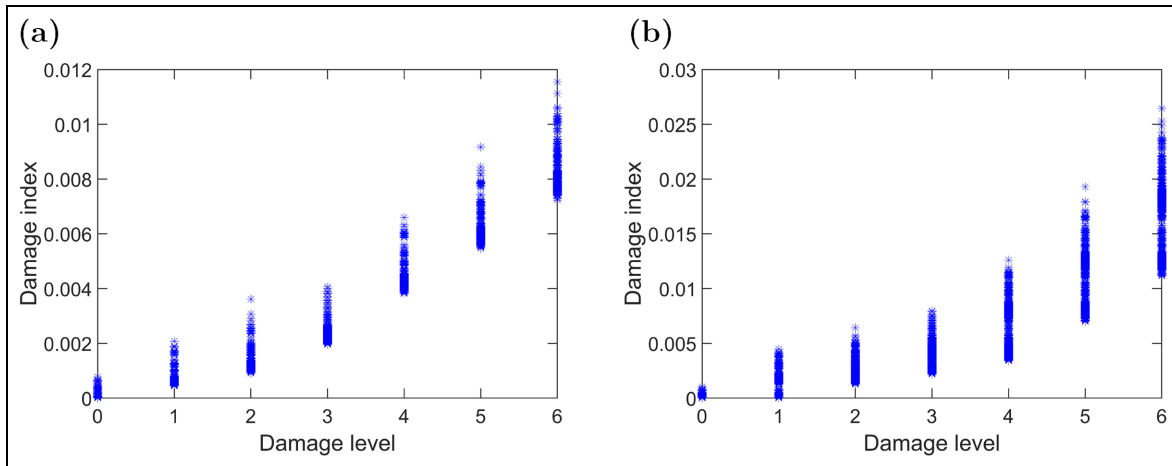


Figure 16. The evolution of the damage index for indicative actuator-sensor paths: (a) damage non-intersecting path 1–4 and (b) damage intersecting path 3–4. Note that the damage index monotonically increases with the increase in damage level both for damage non-intersecting path 1–4 and damage intersecting path 3–4. However, a great deal of overlapping of the magnitude of the damage indices exists between different damage levels, which makes damage identification difficult.

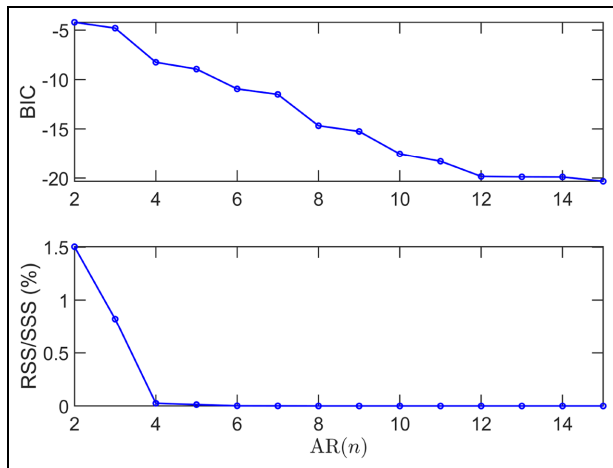


Figure 17. Model order selection via the BIC (top) and RSS/SSS (bottom) criteria for the CFRP plate for damage non-intersecting path 1–4. Note that similar to the case of the aluminum plate, the BIC criterion suggests $n_a = 12$ and the RSS/SSS criterion suggests $n_a = 4$ for the AR model order.
AR: autoregressive; BIC: Bayesian information criterion; CFRP: carbon fiber reinforced plastic; RSS: residual sum of squares; SSS: signal sum of squares.

a particular damage detection method, which fall along this line are no better than a random guess. Methods that generate points below this line are bad predictors or classifiers. The upper left corner of the ROC space with a coordinate (0,1) represents 100% sensitivity, that is, no false negative, and 100% specificity, that is, no false positives. As such, this point is called perfect classification. In Figure 27(a), (b), and (d), the red line passes through the point (0,1) which means perfect

detection capability has been achieved. In addition, in Figure 27(c), the red line does not pass through the point (0,1), which means the damage detection method used in this case may not achieve perfect detection capability. In general, for the CFRP plate, in terms of damage detection, the damage non-intersecting path 1–4 perform better than the damage intersecting path 3–4, the exact opposite of the case of the aluminum plate.

Discussion

In this paper, a stationary stochastic time-series model, namely the AR model is employed in the context of ultrasonic guided wave-based damage detection and identification. Ultrasonic guided waves or Lamb waves can be generated in plate-like structures and show dispersive behavior during propagation. That is, waves of different wavelengths (frequencies) travel at different phase velocities. Traditionally, the first symmetric (S_0) or the anti-symmetric mode (A_0) or the first arrival wave packet, which is free from the effect of boundary and reflection, is used to determine the existence, location, and severity of the damage in the structure. However, in many practical situations, when the actuating and receiving sensors are mounted close to the boundary of the structure, and complex boundary conditions are present, it may not always be possible to have a reflection-free S_0 , A_0 , or first arrival wave packet. In addition, it is extremely difficult to exactly isolate the S_0 or the A_0 mode from the received waveform signal. For example, in Figure 2(c) and Figure 15(c), top subplot, it is hard to determine which part is S_0 and A_0 mode. In addition, in Figure 2(c), top

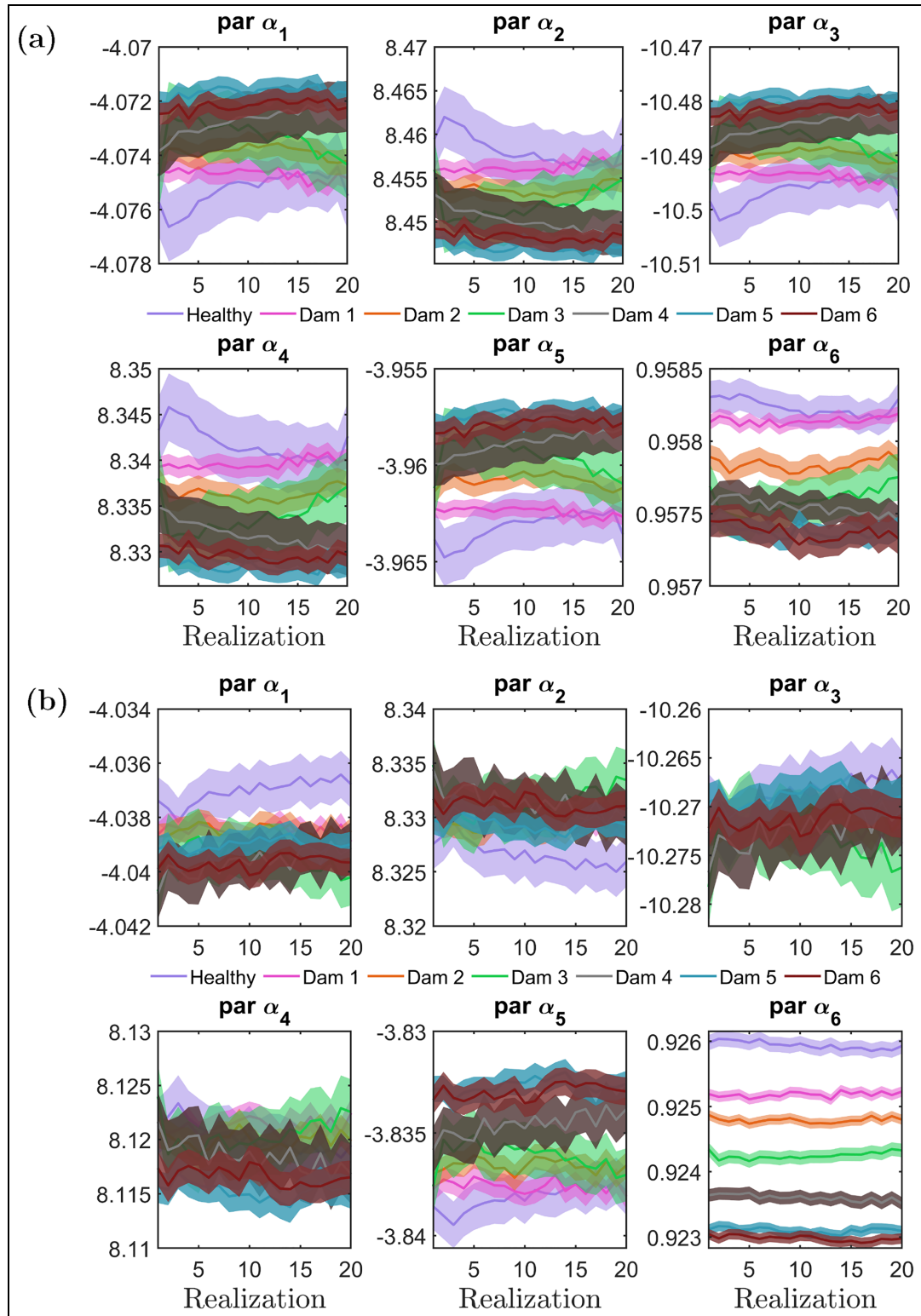


Figure 18. AR(6) model parameters for different structural states for the CFRP plate: the parameter mean is shown as solid lines and the associated ± 2 standard deviations as shaded regions; (a) damage intersecting path 3–4 and (b) damage non-intersecting path 1–4. Note that for the case of the CFRP plate, the parameters of both the damage intersecting path 3–4 as well as damage non-intersecting path 1–4 are overlapping, which makes damage identification more challenging.
AR: autoregressive; CFRP: carbon fiber reinforced plastic.

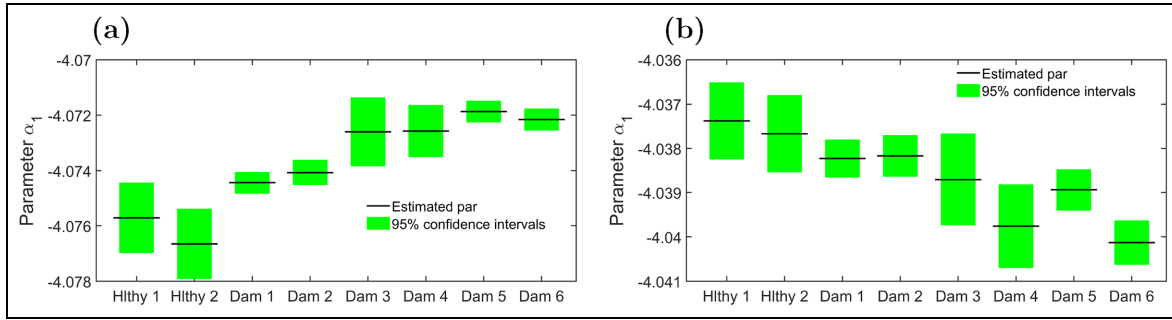


Figure 19. Estimated model parameters for healthy and damaged states and the corresponding 95% confidence intervals of the CFRP coupon: (a) parameter α_1 for damage intersecting path 3–4 and (b) parameter α_1 for damage non-intersecting path 1–4. Note that the confidence bound for the parameter α_1 is overlapping among different damage levels, both for damage intersecting path 3–4 and damage non-intersecting path 1–4, which may complicate damage detection and identification.
CFRP: carbon fiber reinforced plastic.

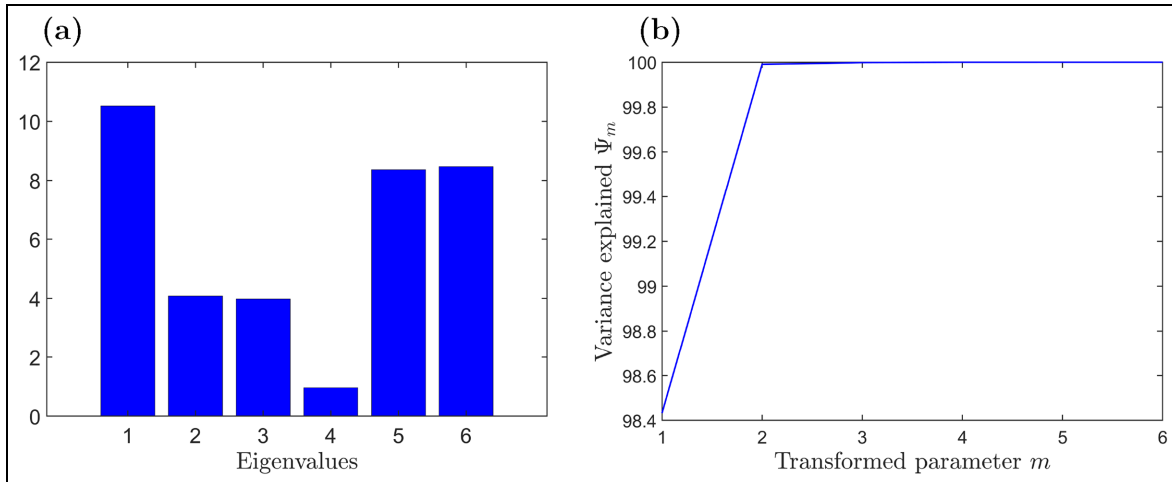


Figure 20. AR parameter selection process for damage diagnosis of the CFRP plate: (a) SVD-based approach and (b) PCA-based approach. Note that the SVD-based method may suggest the use of five parameters corresponding to the five eigenvalues, whose magnitude is greater than 2. On the other hand, the PCA-based approach may suggest the use of only two parameters, as two parameters can explain 99.9% variance.

AR: autoregressive; CFRP: carbon fiber reinforced plastic; SVD: singular value decomposition; PCA: principal component analysis.

subplot, it is the reflection part where the effect of damage is clearly visible (between 230 and 330 μs). As a result, excluding the reflection part from the analysis may reduce the ability to detect damage efficiently within the structure.

In the present work, the proposed method does not exclude any part of the received ultrasonic signal or require any extensive preprocessing to implement (which is usually the case for most artificial neural network-based approaches). Rather, this method focuses on the underlying dynamics or the change in the dynamics of the received signal due to the presence of damage. The extraction of the underlying dynamics is achieved through autoregressive modeling and

invoking the principles of the system identification framework.

However, AR models are founded upon certain assumptions. The violations of these assumptions may lead to incorrect conclusions. Among these assumptions, the most important one is the assumption of stationarity, that is, the signal mean and variance do not change with time. Another assumption is the use of a Gaussian white noise actuation, which ensures the persistence of excitation of the system, and uncorrelated Gaussian residuals when the system has been modeled properly.

In the present work, the above-mentioned two assumptions have been relaxed to a certain extent. Ultrasonic guided waves are nonstationary signals.

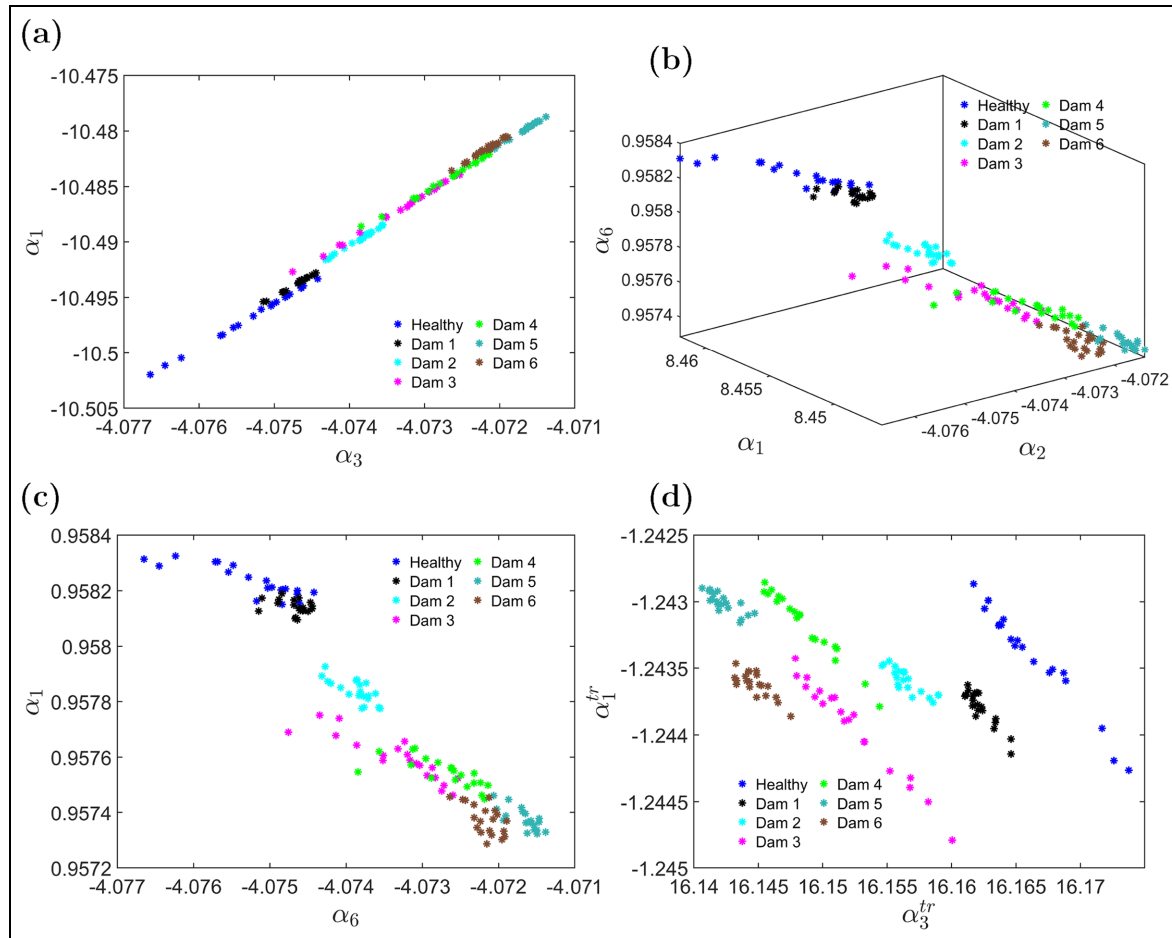


Figure 21. Indicative AR(6) model parameters of the CFRP coupon are shown for damage non-intersecting path I–4: (a) model parameters α_1 and α_2 , (b) model parameters α_1 , α_2 , and α_6 , (c) model parameters to be used in damage detection indicated by the SVD-based approach (α_1 and α_6), and (d) truncated model parameters from PCA transformation. Note that after the SVD and PCA transformation, the overlapping of the model parameters between different damage levels gets reduced.

AR: autoregressive; CFRP: carbon fiber reinforced plastic; SVD: singular value decomposition; PCA: principal component analysis.

Although the mean remains constant, the variance change with time. The present study explores the relaxation of the non-stationarity assumption by deploying stationary autoregressive models. It was found that guided waves are weakly nonstationary. As a result, in spite of using stationary autoregressive models, the underlying dynamics can be captured and damage detection and identification can be performed quite nicely. Both metallic and composite coupons were used to demonstrate the method's versatility for damage diagnosis. In addition, SVD- and PCA-based dimensionality reduction techniques on model parameters were also used. This may especially be useful when the system has a large number of parameters.

Another relaxation of assumption was to use narrow band 5-peak tone burst actuation instead of a random Gaussian white noise actuation. Five-peak tone burst is

a typical actuation signal in ultrasonic guided wave-based damage diagnosis. It was found in this paper that the AR modeling of the resulting response signals due to this actuation did not render the identification of the system intractable. The details of the damage diagnosis results in both metallic and composite coupons are summarized in Tables 5 and 8. The AR-based damage diagnosis approach shown in this study infers that invoking nonlinear models such as the nonlinear autoregressive with exogenous excitation (NARX) model may complicate the damage diagnosis process and may impart unnecessary computational burden.

It is to be mentioned here that when performing parameter estimation of the AR model from available data, it is recommended to use WLS or maximum likelihood estimators, which are unbiased and asymptotically efficient.

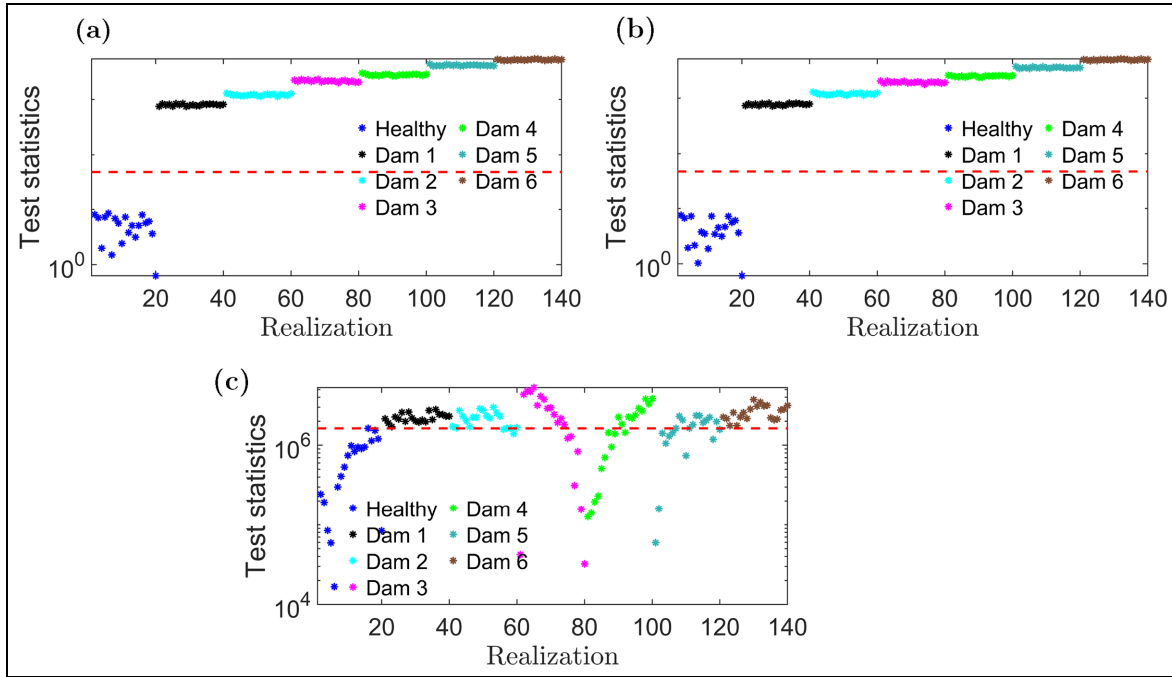


Figure 22. Damage detection performance comparison for damage intersecting path 3–4 for the CFRP plate using the covariance matrix derived from 20 experimental healthy signals: (a) standard AR approach, (b) SVD-based approach, and (c) PCA-based approach. Note that for damage intersecting path 3–4 and experimental covariance matrix, both the standard AR and SVD-based approaches perform well for damage detection, as the healthy test statistics remain below the threshold. However, the PCA-based approach performs badly in this case.

AR: autoregressive; CFRP: carbon fiber reinforced plastic; SVD: singular value decomposition; PCA: principal component analysis.

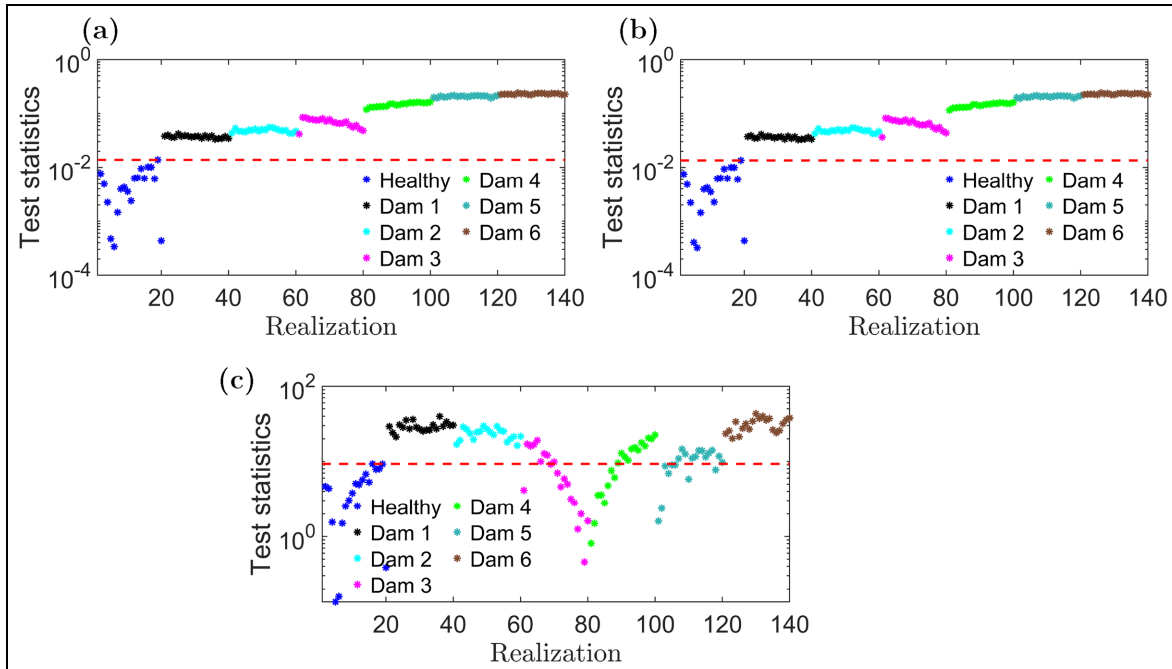


Figure 23. Damage detection performance comparison for damage intersecting path 3–4 for the CFRP plate using the AR(6)-based covariance matrix: (a) standard AR approach, (b) SVD-based approach, and (c) PCA-based approach. Note that for damage intersecting path 3–4 and AR(6)-based covariance matrix, both the standard AR and SVD-based approaches perform well, although the test statistics are more closely spaced between different damage levels. The PCA-based approach shows poor damage detection performance.

AR: autoregressive; CFRP: carbon fiber reinforced plastic; SVD: singular value decomposition; PCA: principal component analysis.

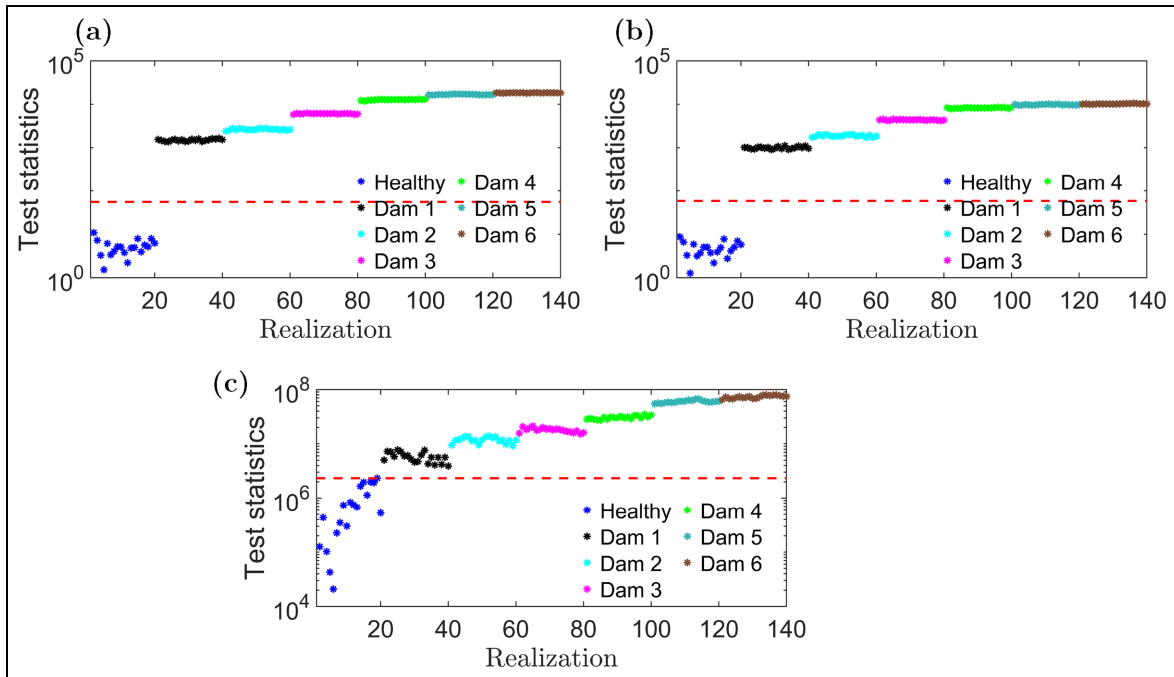


Figure 24. Damage detection performance for damage non-intersecting path I–4 for the CFRP plate using the covariance matrix derived from 20 experimental healthy signals: (a) standard AR approach, (b) SVD-based approach, and (c) PCA-based approach. Note that for damage non-intersecting path I–4 and experimental covariance matrix, all three approaches perform well in the CFRP plate. AR: autoregressive; CFRP: carbon fiber reinforced plastic; SVD: singular value decomposition; PCA: principal component analysis.

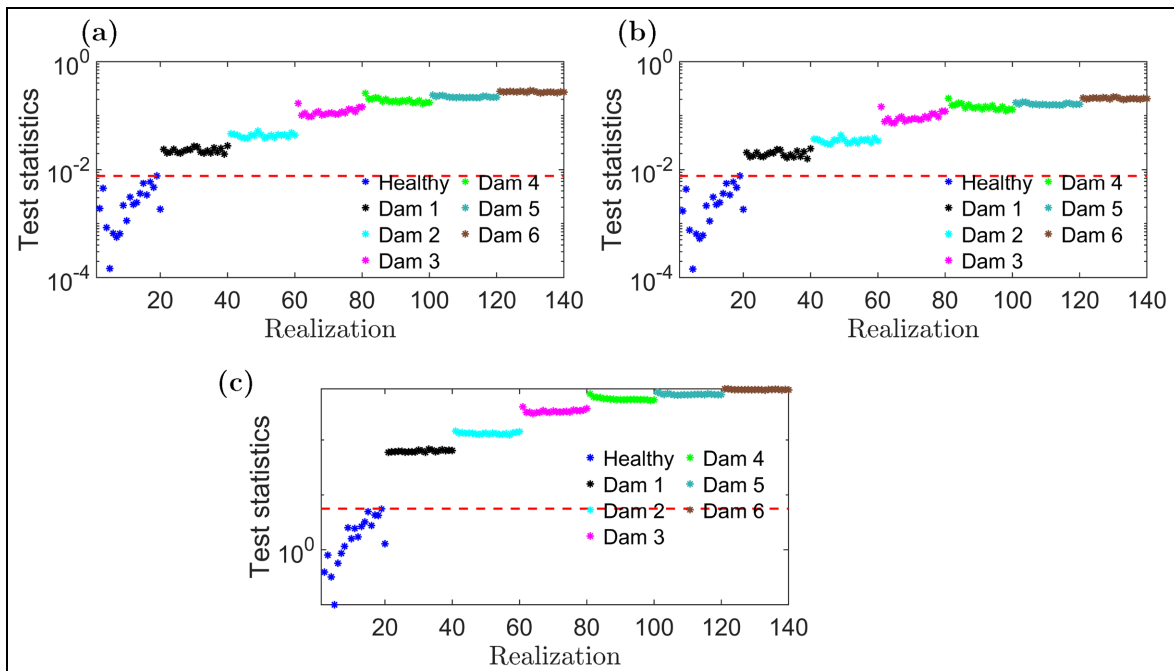


Figure 25. Damage detection performance comparison for damage non-intersecting path I–4 for the CFRP plate using the AR(6)-based covariance matrix: (a) standard AR approach, (b) SVD-based approach, and (c) PCA-based approach. Note that for damage non-intersecting path I–4 and AR(6)-based covariance matrix, all three approaches perform well for damage detection, although the test statistics are closely spaced between different damage levels.

AR: autoregressive; CFRP: carbon fiber reinforced plastic; SVD: singular value decomposition; PCA: principal component analysis.

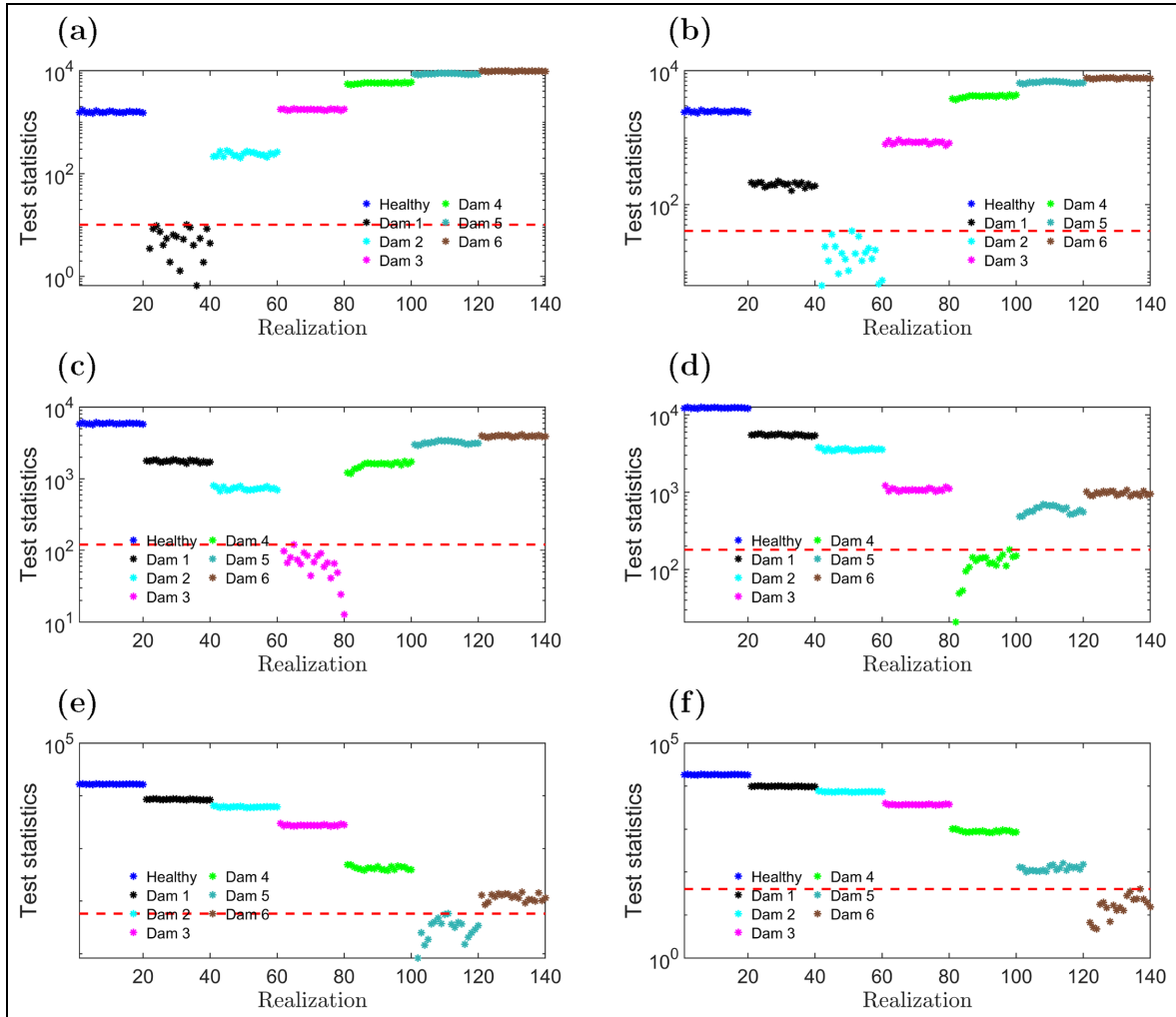


Figure 26. Damage identification results for the CFRP plate using damage non-intersecting path 1–4 for the standard AR-based approach and using the covariance matrix derived from 20 healthy signals: (a) damage level 1, (b) damage level 2, (c) damage level 3, (d) damage level 4, (e) damage level 5, and (f) damage level 6. Note that perfect damage identification has been achieved for damage non-intersecting path 1–4 using the standard AR-based approach and experimental covariance matrix.
AR: autoregressive; CFRP: carbon fiber reinforced plastic.

Conclusion

The objective of this work was the formulation and numerical assessment of a statistical damage diagnostic scheme in the context of ultrasonic guided wave-based damage diagnosis using stationary AR models. These are output-only stochastic models and automatically account for uncertainties. In addition to using standard AR-based damage detection and identification where all the parameters were used without any modifications, two additional methods were also investigated where the model parameters were modified to simplify the damage detection algorithm. One approach was an SVD-based approach where model parameters were

sorted according to the magnitude of the eigenvalues obtained from the parameter matrix. Another approach was a PCA-based truncation approach where model parameters were projected onto a lower-dimensional subspace. These methods were tested on an aluminum plate as well as on a composite coupon for different damage scenarios and different paths. It was found that for the case of the aluminum plate, all three methods work for damage detection and identification. On the other hand, for the CFRP plate, the methods presented in the paper partially work. Perfect damage identification remains challenging with the current framework for composites. This issue will be

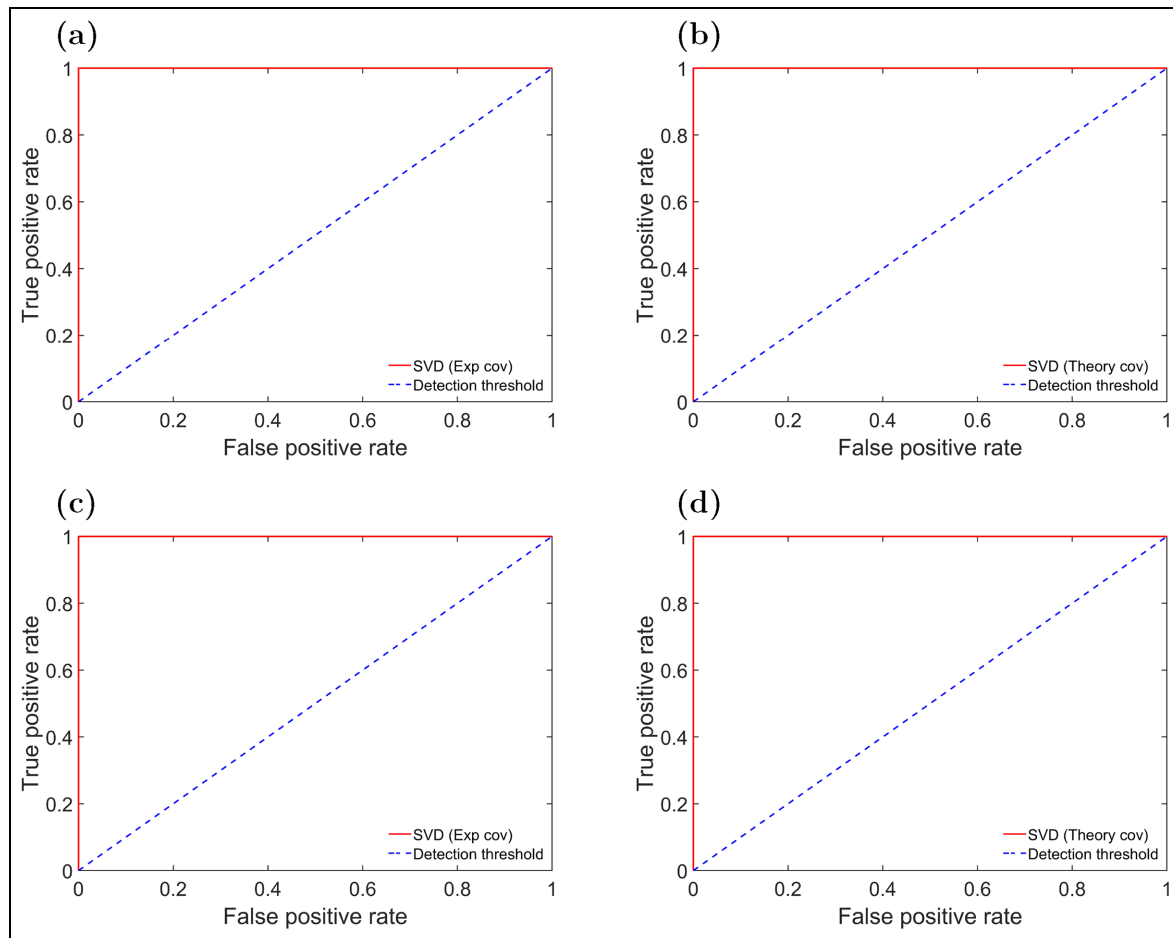


Figure 27. ROC plots comparing the SVD-based damage detection methods for the CFRP plate for different paths and covariance used: (a) path 1–4 with the experimental covariance, (b) path 1–4 with the AR(6)-based covariance, (c) path 3–4 with the experimental covariance, and (d) path 3–4 with the AR(6)-based covariance. Here, the dotted blue diagonal line represents the discrimination threshold. The red line represents the damage detection capability of the method. Note that perfect detection was achieved for (a), (b), and (d), as the red line passes through the point (0,1), the point of perfect classification.
AR: autoregressive; CFRP: carbon fiber reinforced plastic; SVD: singular value decomposition; ROC: receiver operating characteristic.

Table 7. The α -level chart for the composite plate.

Method	Path	Covariance	α -level
Standard AR	1–4	Experiment	1×10^{-10}
	1–4	Theory	Manual
	2–6	Experiment	1×10^{-9}
	2–6	Theory	Manual
SVD based	1–4	Experiment	1×10^{-10}
	1–4	Theory	Manual
	2–6	Experiment	1×10^{-9}
	2–6	Theory	Manual
PCA based	1–4	Experiment	Manual
	1–4	Theory	Manual
	2–6	Experiment	Manual
	2–6	Theory	Manual
			0.09

AR: autoregressive; SVD: singular value decomposition; PCA: principal component analysis.

Table 8. Damage detection and identification summary results for the CFRP plate.

Method	Path	Covariance	Damage detection								
			False alarms	Healthy	Missed damage	Damage 1	Damage 2	Damage 3	Damage 4	Damage 5	Damage 6
Damage detection											
Standard AR	1-4	Experiment	0/20	0/20	0/20	0/20	0/20	0/20	0/20	0/20	0/20
	1-4	Theory	0/20	0/20	0/20	0/20	0/20	0/20	0/20	0/20	0/20
SVD based	3-4	Experiment	0/20	7/20	0/20	0/20	0/20	0/20	0/20	0/20	0/20
	3-4	Theory	0/20	0/20	0/20	0/20	0/20	0/20	0/20	0/20	0/20
SVD based	1-4	Experiment	0/20	0/20	0/20	0/20	0/20	0/20	0/20	0/20	0/20
	1-4	Theory	0/20	0/20	0/20	0/20	0/20	0/20	0/20	0/20	0/20
PCA based	3-4	Experiment	0/20	20/20	20/20	4/20	4/20	0/20	0/20	0/20	0/20
	1-4	Theory	0/20	0/20	0/20	0/20	0/20	0/20	0/20	0/20	0/20
PCA based	3-4	Experiment	0/20	0/20	0/20	0/20	0/20	0/20	0/20	0/20	0/20
	3-4	Theory	0/20	0/20	0/20	0/20	0/20	0/20	0/20	0/20	0/20
Damage identification											
Method	Path	Covariance	Damage identification								
			Damage misclassification	Damage 1	Damage 2	Damage 3	Damage 4	Damage 5	Damage 6		
Standard AR	1-4	Experiment	(-,0,0,0,0)	(0,-,0,0,0)	(0,0,-,0,0)	(0,0,0,-,0)	(0,0,0,0,-)	(0,0,0,0,0)	(0,0,0,0,0)	(0,0,0,0,0)	
	1-4	Theory	(-,0,0,0,0)	(0,-,0,0,0)	(0,0,-,0,0)	(0,0,0,-,0)	(0,0,0,0,-)	(0,0,0,0,0)	(0,0,0,0,0)	(0,0,0,0,0)	
SVD based	3-4	Experiment	(-,0,0,0,0)	(0,-,0,0,0)	(0,0,-,0,0)	(0,0,0,-,0)	(0,0,0,0,-)	(0,0,0,0,0)	(0,0,0,0,0)	(0,0,0,0,0)	
	3-4	Theory	(-,12,0,0,0)	(20,-,0,0,0)	(20,20,-,2,0,0)	(0,0,5,-,0)	(0,0,0,-,5)	(0,0,0,0,-)	(0,0,0,0,-)	(0,0,0,0,-)	
SVD based	1-4	Experiment	(-,0,0,0,0)	(0,-,0,0,0)	(0,0,-,0,0)	(0,0,0,-,18,1)	(0,0,0,-,13)	(0,0,0,0,-)	(0,0,0,0,-)	(0,0,0,0,-)	
	1-4	Theory	(-,0,0,0,0)	(0,-,0,0,0)	(0,0,-,0,0)	(0,0,8,-,0)	(0,0,0,-,0)	(0,0,0,0,-)	(0,0,0,0,-)	(0,0,0,0,-)	
PCA based	3-4	Experiment	(-,0,0,0,0)	(0,-,0,0,0)	(0,0,-,0,0)	(0,0,0,-,0)	(0,0,0,-,0)	(0,0,0,0,-)	(0,0,0,0,-)	(0,0,0,0,-)	
	3-4	Theory	(-,12,0,0,0)	(20,-,0,0,0)	(20,20,-,2,0,0)	(0,1,6,-,0)	(0,0,0,-,9)	(0,0,0,0,-)	(0,0,0,0,-)	(0,0,0,0,-)	
PCA based	1-4	Experiment	(-,0,0,0,0)	(19,-,0,0,0)	(0,4,-,10,0)	(0,0,20,-,0,0)	(0,0,0,-,10)	(0,0,0,0,-)	(0,0,0,0,-)	(0,0,0,0,-)	
	1-4	Theory	(-,0,0,0,0)	(0,-,0,0,0)	(0,0,-,0,0)	(0,0,0,-,1)	(0,0,0,-,1)	(0,0,0,0,-)	(0,0,0,0,-)	(0,0,0,0,-)	
3-4	Experiment	(-,13,0,0,0)	(20,-,4,2,2,20)	(20,20,-,20,20)	(11,15,0,11,-7)	(20,20,-,20,20)	(11,15,0,11,-7)	(20,15,1,0,-)	(20,15,1,0,-)		
	3-4	Theory	(-,6,0,0,13)	(20,-,1,0,19)	(20,20,-,16,20,19)	(1,8,20,-,20,3)	(1,8,20,-,20,3)	(20,18,0,0,-)	(20,18,0,0,-)		

AR: autoregressive; CFRP: carbon fiber reinforced plastic; SVD: singular value decomposition; PCA: principal component analysis.

resolved in the future paper by the authors using time-varying time-series models.

The methods presented in the current paper for damage detection and identification for guided wave-based SHM are mathematically simple, computationally inexpensive, statistical in nature, and easy to use. In addition, these methods can potentially be automated to develop smart and intelligent structural systems.

Declaration of conflicting interests

The author(s) declared no potential conflicts of interest with respect to the research, authorship, and/or publication of this article.

Funding

The author(s) disclosed receipt of the following financial support for the research, authorship, and/or publication of this article: This work is supported by the U.S. Air Force Office of Scientific Research (AFOSR) grant “Formal Verification of Stochastic State Awareness for Dynamic Data-Driven Intelligent Aerospace Systems” (FA9550-19-1-0054) with Program Officer Dr. Erik Blasch.

ORCID iDs

Shabbir Ahmed  <https://orcid.org/0000-0001-8296-6025>
Fotis Kopsaftopoulos  <https://orcid.org/0000-0001-8795-3725>

References

1. Kopsaftopoulos F and Chang F-K. A dynamic data-driven stochastic state-awareness framework for the next generation of bio-inspired fly-by-feel aerospace vehicles. In: Blasch E, Ravela S and Aved A (eds) *Handbook of dynamic data driven applications systems*. Cham: Springer International Publishing, 2018, pp. 697–721.
2. Kopsaftopoulos F and Fassois S. Vibration based health monitoring for a lightweight truss structure: experimental assessment of several statistical time series methods. *Mech Syst Signal Process* 2010; 24(7): 1977–1997.
3. Janapati V, Kopsaftopoulos F, Li F, et al. Damage detection sensitivity characterization of acousto-ultrasound-based structural health monitoring techniques. *Struct Health Monit* 2016; 15(2): 143–161.
4. Ihn J and Chang F-K. Pitch-catch active sensing methods in structural health monitoring for aircraft structures. *Struct Health Monit* 2008; 7(1): 5–19.
5. Amer A and Kopsaftopoulos F. Gaussian process regression for active sensing probabilistic structural health monitoring: experimental assessment across multiple damage and loading scenarios. *arXiv preprint arXiv:2106.14841*, 2021.
6. Sodano HA. Development of an automated eddy current structural health monitoring technique with an extended sensing region for corrosion detection. *Struct Health Monit* 2007; 6(2): 111–119.
7. Dubuc B, Sitaropoulos K, Ebrahimkhanlou A, et al. Acoustic emission diagnostics of corrosion monitoring in prestressed concrete using hidden markov and semi-markov models. *Struct Health Monit* 2021; 20(6): 2899–2916.
8. Reilly JP. *A temperature driven method for structural health monitoring*. PhD Thesis, Princeton University, 2019.
9. Fassois SD. Parametric identification of vibrating structures. In: Braun S, Ewins D and Rao S (eds) *Encyclopedia of vibration*, Cambridge, Massachusetts: Academic Press, 2001, pp. 673–685.
10. Fassois SD and Sakellariou JS. Time-series methods for fault detection and identification in vibrating structures. *Philos Trans Royal Soc. A PHILOS T R SOC A* 2007; 365(1851): 411–448.
11. Kopsaftopoulos FP and Fassois SD. A functional model based statistical time series method for vibration based damage detection, localization, and magnitude estimation. *Mech Syst Signal Process* 2013; 39(1–2): 143–161.
12. Avendaño-Valecia LD, Chatzi EN, Koo KY, et al. Gaussian process time-series models for structures under operational variability. *Front Built Environ* 2017; 3: 69.
13. Kopsaftopoulos FP and Fassois SD. A stochastic functional model based method for vibration based damage detection, localization, and magnitude estimation. *Mech Syst Signal Process* 2013; 39: 143–161.
14. Roy S, Lonkar K, Janapati V, et al. A novel physics-based temperature compensation model for structural health monitoring using ultrasonic guided waves. *Struct Health Monit* 2014; 13(3): 321–342.
15. Ihn J and Chang F-K. Detection and monitoring of hidden fatigue crack growth using a built-in piezoelectric sensor/actuator network, part I: diagnostics. *Smart Mater Struct* 2004; 13: 609–620.
16. Ihn J and Chang F-K. Detection and monitoring of hidden fatigue crack growth using a built-in piezoelectric sensor/actuator network, part II: validation through riveted joints and repair patches. *Smart Mater Struct* 2004; 13: 621–630.
17. Amer A and Kopsaftopoulos FP. Statistical guided-waves-based structural health monitoring via stochastic non-parametric time series models. *Struct Health Monit* 2021; 1–28.
18. Amer A, Roy S and Kopsaftopoulos FP. Probabilistic SHM under varying loads via the integration of Gaussian process regression and physics-based guided-wave propagation models. In: *Proceedings of the AIAA SciTech 2021 Forum, (Virtual Event)*, 2021.
19. Song G, Gu H and Mo Y-L. Smart aggregates: multi-functional sensors for concrete structures—a tutorial and a review. *Smart Mater Struct* 2008; 17(3): 033001.
20. Wang F, Huo L and Song G. A piezoelectric active sensing method for quantitative monitoring of bolt loosening using energy dissipation caused by tangential damping based on the fractal contact theory. *Smart Mater Struct* 2017; 27(1): 015023.
21. Tibaduiza DA, Mujica LE, Rodellar J, et al. Structural damage detection using principal component analysis and damage indices. *J Intelligent Mater Syst Struct* 2016; 27(2): 233–248.

22. Lizé E, Rébillat M, Mechbal N, et al. Optimal dual-PZT sizing and network design for baseline-free shm of complex anisotropic composite structures. *Smart Mater Struct* 2018; 27(11): 115018.
23. Qiu J, Li F, Abbas S, et al. A baseline-free damage detection approach based on distance compensation of guided waves. *J Low Freq Noise Vibr Act Control* 2019; 38(3–4): 1132–1148.
24. Segers J, Hedayatrasa S, Poelman G, et al. Nonlinear local wave-direction estimation for in-sight and out-of-sight damage localization in composite plates. *NDT & E Int* 2021; 119: 102412.
25. Cantero-Chinchilla S, Chiachio J, Chiachio M, et al. A robust bayesian methodology for damage localization in plate-like structures using ultrasonic guided-waves. *Mech Syst Signal Process* 2019; 122: 192–205.
26. Jin H, Yan J, Li W, et al. Monitoring of fatigue crack propagation by damage index of ultrasonic guided waves calculated by various acoustic features. *Appl Sci* 2019; 9(20): 4254.
27. Xu B, T Zhang, Song G, et al. Active interface debonding detection of a concrete-filled steel tube with piezoelectric technologies using wavelet packet analysis. *Mech Syst Signal Process* 2013; 36(1): 7–17.
28. Hua J, Cao X, Yi Y, et al. Time-frequency damage index of broadband lamb wave for corrosion inspection. *J Sound Vib* 2020; 464: 114985.
29. Su Z, Zhou C, Hong M, et al. Acousto-ultrasonics-based fatigue damage characterization: linear versus nonlinear signal features. *Mech Syst Signal Process* 2014; 45(1): 225–239.
30. Ibáñez F, Baltazar A and Mijarez R. Detection of damage in multiwire cables based on wavelet entropy evolution. *Smart Mater Struct* 2015; 24(8): 085036.
31. Rojas E, Baltazar A and Loh K. Damage detection using the signal entropy of an ultrasonic sensor network. *Smart Mater Struct* 2015; 24(7): 075008.
32. Qiu L, Fang F, Yuan S, et al. An enhanced dynamic gaussian mixture model-based damage monitoring method of aircraft structures under environmental and operational conditions. *Struct Health Monit* 2019; 18(2): 524–545.
33. Haynes C, Todd MD, Flynn E, et al. Statistically-based damage detection in geometrically-complex structures using ultrasonic interrogation. *Struct Health Monit* 2013; 12(2): 141–152.
34. Ahmed S and Kopsaftopoulos F. Stochastic identification of guided wave propagation under ambient temperature via non-stationary time series models. *Sensors* 2021; 21(16): 5672.
35. Ahmed S and Kopsaftopoulos F. Time-varying identification of guided wave propagation under varying temperature via non-stationary time series models. *arXiv preprint arXiv:2201.04721*, 2022.
36. Ahmed S and Kopsaftopoulos F. Active sensing acousto-ultrasound shm via stochastic non-stationary time series models. In: *European workshop on structural health monitoring*, 2023, pp. 256–266. Palermo, Italy: Springer.
37. Ahmed S and Kopsaftopoulos F. Active sensing acousto-ultrasound SHM via stochastic time series models. In: *Health Monitoring of Structural and Biological Systems XVI*, 2022, vol. 12048, pp. 358–366. Long Beach, California: SPIE.
38. Kopsaftopoulos FP and Fassois SD. Experimental assessment of time series methods for structural health monitoring (SHM). In: *Proceedings of the 4th European workshop on structural health monitoring (EWSHM)*, Cracow, Poland, 2008.
39. Kopsaftopoulos FP and Fassois SD. Vibration-based structural damage detection and precise assessment via stochastic functionally pooled models. *Key Eng Mater* 2007; 347: 127–132.
40. Kopsaftopoulos FP and Fassois SD. Identification of stochastic systems under multiple operating conditions: the vector dependent FP-ARX parametrization. In: *Proceedings of 14th mediterranean conference on control and automation*, Ancona, Italy, 2006.
41. Kopsaftopoulos FP and Fassois SD. Vibration-based fault detection and assessment in a scale aircraft structure via stochastic VFP-ARX models. In: *Proceedings of the 3rd European workshop on structural health monitoring (EWSHM)*, Granada, Spain, 2006.
42. Kopsaftopoulos FP, Magripis SG, Amplianitis AD, et al. Scalar and vector time series methods for vibration based damage diagnosis in an aircraft scale skeleton structure. In: *Proceedings of the ASME 2010 10th biennial conference on engineering systems design and analysis*, Istanbul, Turkey, 2010.
43. Kopsaftopoulos F, Nardari R, Li Y-H, et al. A stochastic global identification framework for aerospace structures operating under varying flight states. *Mech Syst Signal Process* 2018; 98: 425–447.
44. Spiridonakos M and Fassois S. Non-stationary random vibration modelling and analysis via functional series time-dependent arma (FS-TARMA) models—a critical survey. *Mech Syst Signal Process* 2014; 47(1–2): 175–224.
45. Spiridonakos M and Fassois S. An FS-TAR based method for vibration-response-based fault diagnosis in stochastic time-varying structures: experimental application to a pick-and-place mechanism. *Mech Syst Signal Process* 2013; 38(1): 206–222.
46. Poulimenos AG and Fassois SD. Output-only stochastic identification of a time-varying structure via functional series tarma models. *Mech Syst Signal Process* 2009; 23(4): 1180–1204.
47. Wang K, Zhang J, Shen Y, et al. Wilcox. Defect detection in guided wave signals using nonlinear autoregressive exogenous method. *Struct Health Monit* 2022; 21(3): 1012–1030.
48. Tu XL, Pyle RJ, Croxford AJ, et al. Potential and limitations of NARX for defect detection in guided wave signals. *Struct Health Monit* 2023; 22(3): 1863–1875.

49. DaSilva S, Villani LG, Rebillat M, et al. Gaussian process NARX model for damage detection in composite aircraft structures. *J Nondestr Eval Diagn Progn Eng Syst* 2002; 5(1): 011007.
50. Ahmed S and Kopsaftopoulos F. Statistical active-sensing structural health monitoring via stochastic time-varying time series models. In: *2022 American Control Conference (ACC)*, Atlanta, Georgia, 2022, pp. 3599–3606.
51. Amer A, Ahmed S and Kopsaftopoulos F. Active-sensing structural health monitoring via statistical learning: an experimental study under varying damage and loading states. In: *European workshop on structural health monitoring*, 2020, pp. 456–468, Springer.
52. Ahmed S, Zhou P and Kopsaftopoulos F. Active-sensing acousto-ultrasound-based rotorcraft structural health monitoring via adaptive functional series models. In: *Proceedings of the vertical flight society 78th annual forum*, Fort Worth, Texas, 2022, USA.
53. Ljung L. *System identification: theory for the user*. 2nd ed. Upper Saddle River, NJ: Prentice-Hall, 1999.
54. Poulimenos A and Fassois S. Parametric time-domain methods for non-stationary random vibration modelling and analysis—a critical survey and comparison. *Mech Syst Signal Process* 2006; 20(4): 763–816.
55. Akaike H. Prediction and entropy. In: Atkinson AC and Fienberg SE (eds) *A celebration of statistics*. New York, USA: Springer, 1985, pp. 1–24.
56. Schwarz G. Estimating the dimension of a model. *Ann Stat* 1978; 6(2): 461–464.
57. Kruger U and Xie L. *Statistical monitoring of complex multivariate processes: with applications in industrial process control*. 1st ed. West Sussex, UK: Wiley & Sons Ltd, 2012.
58. Fassois SD and Kopsaftopoulos FP. Statistical time series methods for vibration based structural health monitoring. In: Ostachowicz W and Güemes JA (eds) *New trends in structural health monitoring*. Berlin: Springer, 2013, pp. 209–264.

Table A1. Nominal material property values at 25°C.

Materials	Property name	Values
Piezo-electric: PZT-5A	Density (ρ)	7750 kg/m ³
	Young's modulus (GPa)	$E_{11} = E_{22} = 60.97$ $E_{33} = 53.19$
	Poisson ratio	$\nu_{13} = \nu_{23} = 0.4402$, $\nu_{12} = 0.35$
Aluminum	Piezoelectric charge constant (m/V)	$d_{31} = d_{32} = 171e - 12$, $d_{33} = 374e - 12$, $d_{15} = d_{24} = 558e - 12$
	Dielectric constant	$\varepsilon_{11} = \varepsilon_{22} = 15.32e - 9$, $\varepsilon_{33} = 15e - 9$
	Density (ρ) (kg/m ³)	2700
Adhesive	Young's modulus (E GPa)	68.9
	Poisson ratio	0.33
	Density (ρ) (kg/m ³)	1100
	Young's modulus (E GPa)	2.19
	Poisson ratio	0.30

PZT, lead zirconate titanate.

Appendix A

Material properties and equations

The established functional relationships are outlined in the following (Table A1).

Properties of piezoelectric materials:

$$\begin{aligned}\rho_{\text{PZT}} &= 7751.80 - 7.26e - 02T \\ E_{11} &= E_{22} = 60.45 + 2.09e - 02T \\ E_{33} &= 52.95 + 9.8e - 03T \\ \nu_{13} &= \nu_{23} = 0.43 + 3e - 04T - 3e - 06T^2 - 1e - 09T^3 \\ \nu_{12} &= 0.35 + 2e - 04T - 8e - 07T^2 + 2e - 09T^3 \\ d_{31} &= d_{32} = 170.78 - 7.1e - 03T + 6e - 04T^2 + 2e - 16T^3 \\ d_{33} &= 369.12 + 1.49e - 01T + 1.9e - 03T^2 - 4e - 09T^3 \\ d_{15} &= d_{24} = 556 + 4.9e - 02T + 2e - 06T^2 - 2e - 09T^3 \\ \varepsilon_{11} &= \varepsilon_{22} = 14.9e - 09 + 1.42e - 11T + 9.74e - 14T^2 + 4.43e - 17T^3 \\ \varepsilon_{33} &= 14.60e - 09 + 1.47e - 11T + 1.18e - 13T^2 - 5.31e - 18T^3\end{aligned}$$

Properties of aluminum:

$$\begin{aligned}E_{\text{Al}} &= 69.62 - 2.63e - 02T \\ \rho_{\text{Al}} &= 2794.60 - 1.84e - 01T \\ \nu_{\text{Al}} &= 0.32 + 3e - 04T\end{aligned}$$

Properties of the adhesive:

$$\begin{aligned}E_{\text{adh}} &= 3.2 - 0.065T + 1.18e - 03T^2 - 7.72e - 06T^3 \\ G_{\text{adh}} &= 1 + 0.001T - 4e - 05T^2\end{aligned}$$

Appendix B

Central limit theorem and a few statistical distributions

The central limit theorem

Let Z_1, Z_2, \dots, Z_n designate mutually independent random variables each with mean μ_k and (finite) variance σ_k^2 . Then for $n \rightarrow \infty$, the distribution of the random variable $X = \sum_{k=1}^n Z_k$ approaches the Gaussian distribution with mean $E\{X\} = \sum_{k=1}^n \mu_k$ and variance $\text{var}[X] = \sum_{k=1}^n \sigma_k^2$ ⁵⁸ (pp. 263).

The χ^2 distribution

Let Z_1, Z_2, \dots, Z_n designate mutually independent, normally distributed random variables each with mean μ_k and standard deviation σ_k . Then the sum:

$$X = \sum_{k=1}^n \left(\frac{Z_k - \mu_k}{\sigma_k} \right)^2 \quad (\text{B1})$$

is said to follow a (central) χ^2 distribution with n degrees of freedom ($X \sim \chi^2(n)$). Its mean and variance are $E\{X\} = n$ and $\text{var}[X] = 2n$, respectively. Notice that imposing p equality constraints among the random variables Z_1, Z_2, \dots, Z_n reduces the set's effective dimensionality, and thus the number of degrees of freedom by p . When $n \rightarrow \infty$, the χ^2 distribution converges to normal distribution⁵⁸ (pp. 263). Let $x \in \mathbf{R}^n$ follow n -variate normal distribution with zero mean and covariance Σ , that is $x \sim \mathcal{N}(0, \Sigma)$. Then the quantity $x^T \Sigma^{-1} x$ follows (central) χ^2 distribution with n degrees of freedom⁵⁸ (pp. 263).

Student's t distribution

Let Z be the standard normal random variable (zero mean and unit variance). Let X follow a (central) χ^2 distribution with n degrees of freedom and be independent of Z . Then the ratio:

$$T = \frac{Z}{\sqrt{\frac{X}{n}}} \quad (\text{B2})$$

is said to follow a Student or t (central) distribution with n degrees of freedom (central because it is based on a central χ^2 distribution). Its mean and variance are $E\{T\} = 0$ ($n > 1$) and $\text{var}[T] = \frac{n}{n-2}$ ($n > 2$), respectively. The central t distribution approaches the standard normal distribution $\mathcal{N}(0, 1)$ as $n \rightarrow \infty$ ⁵⁸ (pp. 264).

Fisher's F distribution

Let X_1, X_2 be mutually independent random variables following (central) χ^2 distributions with n_1, n_2 degrees of freedom, respectively. Then the ratio:

$$F = \frac{\frac{X_1}{n_1}}{\frac{X_2}{n_2}} \quad (\text{B3})$$

is said to follow a (central) F distribution with n_1, n_2 degrees of freedom ($F \sim \mathcal{F}(n_1, n_2)$); central because it is based on central χ^2 distributions. Its mean and variance are $E\{F\} = \frac{n_2}{n_2 - 2}$ ($n_2 > 2$) and $\text{var}[F] = \frac{2n_2^2(n_1 + n_2 - 2)}{n_1(n_2 - 2)^2(n_2 - 4)}$ ($n_2 > 4$), respectively. Note that for the distribution's $1 - \alpha$ critical point $f_{1-\alpha}(n_1, n_2) = \frac{1}{f_\alpha(n_2, n_1)}$. The (central) F distribution approaches normality as $n_1, n_2 \rightarrow \infty$. On the other hand, when $n_2 \rightarrow \infty$, then $n_1 F$ approaches a (central) χ^2 distribution with n_1 degrees of freedom⁵⁸ (pp. 264).

Appendix C

Additional figures

Figures C1 to C3.

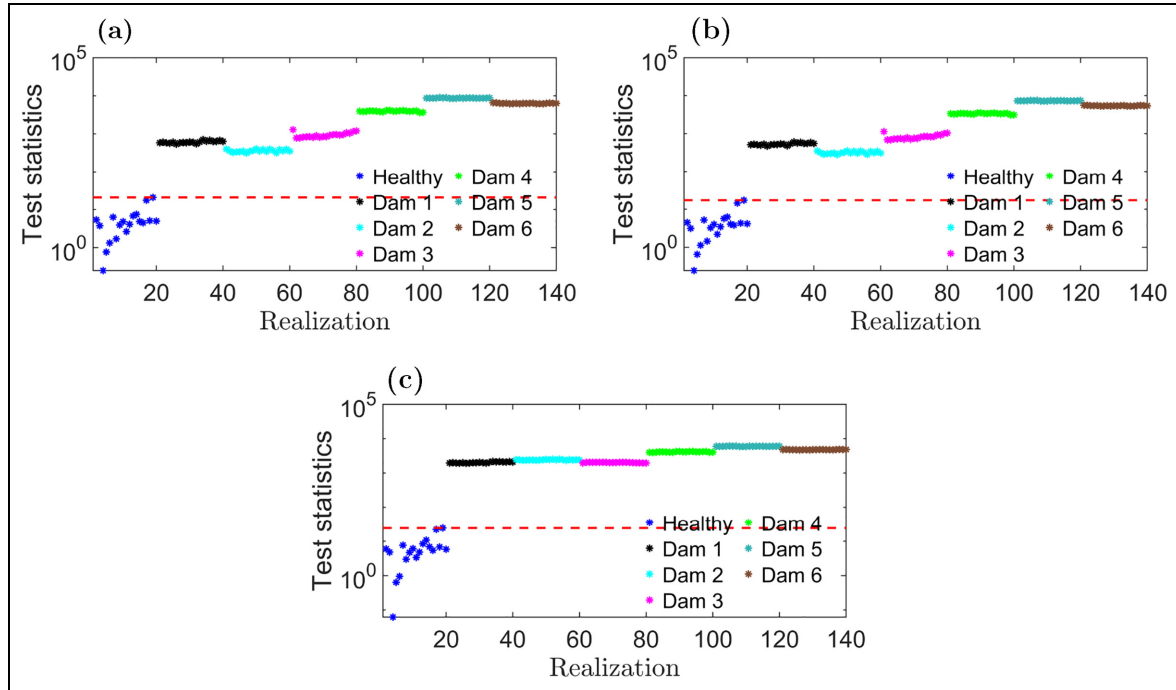


Figure CI. Damage detection performance comparison for damage intersecting path 5–2 for the CFRP plate using the covariance matrix derived from 20 experimental healthy signals: (a) standard AR approach, (b) SVD-based approach, and (c) PCA-based approach. Note that for damage intersecting path 5–2 and experimental covariance matrix, all three approaches perform well. AR: autoregressive; CFRP: carbon fiber reinforced plastic; SVD: singular value decomposition; PCA: principal component analysis.

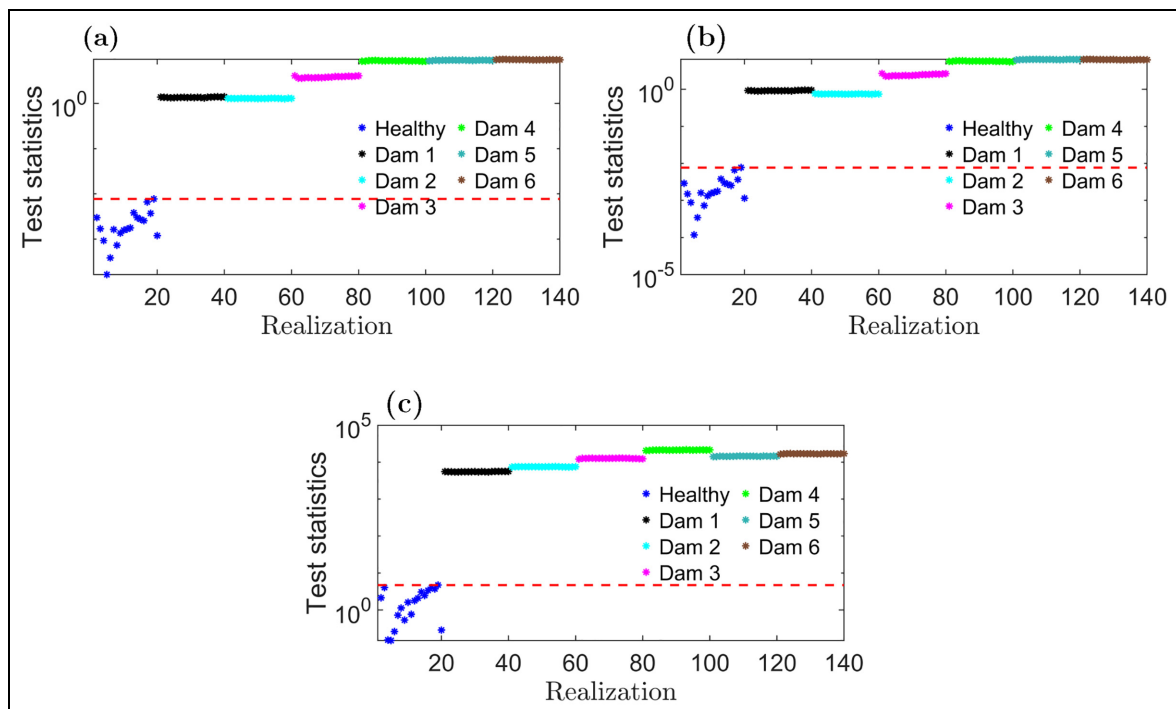


Figure C2. Damage detection performance comparison for damage intersecting path 5–2 for the CFRP plate using the AR(6)-based covariance matrix: (a) standard AR approach, (b) SVD-based approach, and (c) PCA-based approach. Note that for damage intersecting path 5–2 and the AR(6)-based covariance matrix, all three approaches perform well. AR: autoregressive; CFRP: carbon fiber reinforced plastic; SVD: singular value decomposition; PCA: principal component analysis.

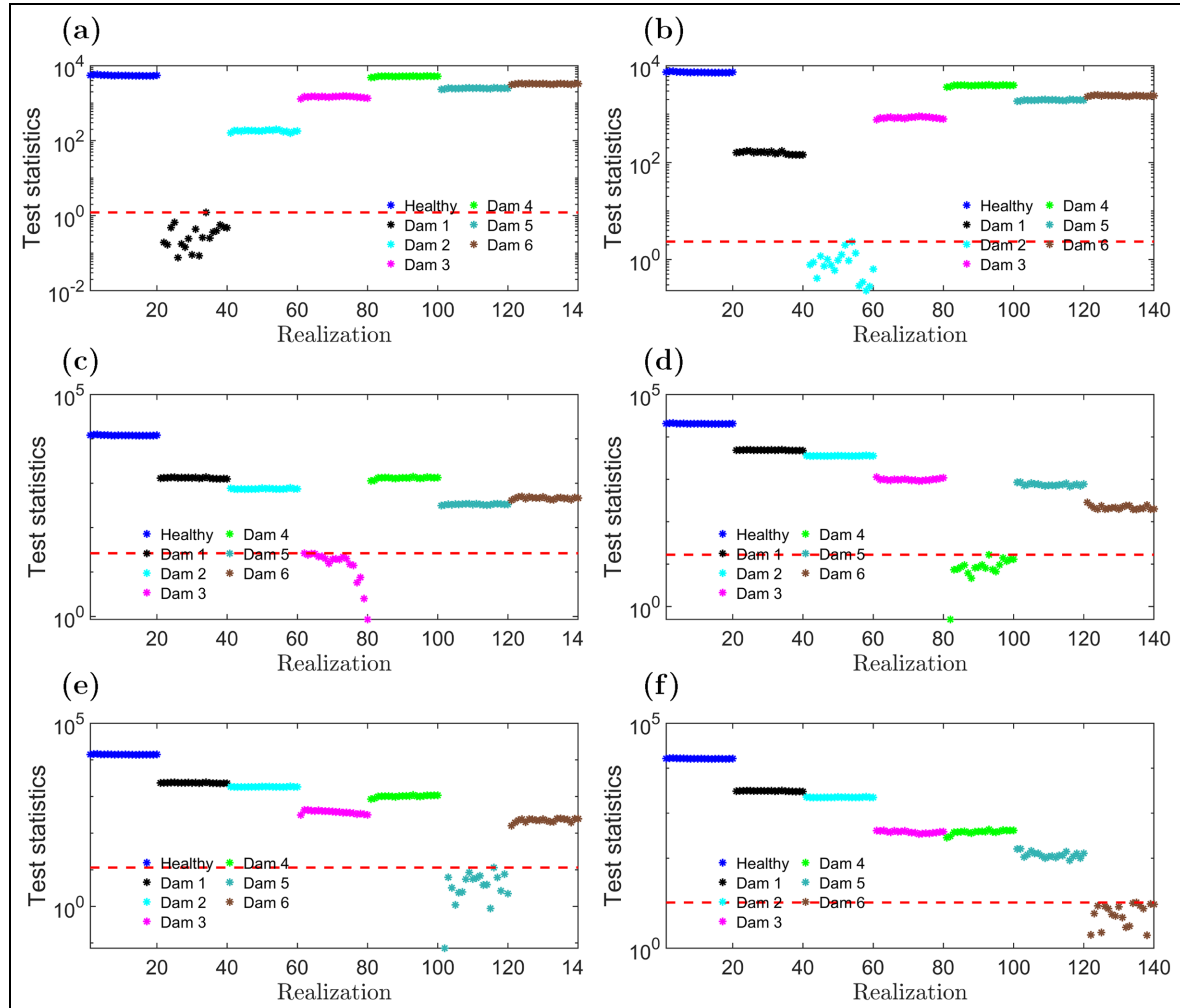


Figure C3. Damage identification results for the CFRP plate using damage intersecting path 5–2 for the PCA-based approach and using AR(6)-based covariance: (a) damage level 1, (b) damage level 2, (c) damage level 3, (d) damage level 4, (e) damage level 5, and (f) damage level 6. Note that for damage intersecting path 5–2 and AR(6)-based covariance matrix, using the PCA-based approach, perfect damage identification has been achieved as the test statistics remain below the threshold for respective damage levels. AR: autoregressive; CFRP: carbon fiber reinforced plastic; PCA: principal component analysis.